THE ASTROPHYSICAL JOURNAL, 414:535–551, 1993 September 10

EFFECTS OF INTERNAL DUST ON THE NARROW-LINE REGION LYMAN AND BALMER DECREMENTS

LUC BINETTE[1] AND JOHN WANG
Canadian Institute for Theoretical Astrophysics, 60 St. George Street, Toronto, Ontario, Canada M5S 1A1
MONTSERRAT VILLAR-MARTIN
Space Telescope—European Coordinating Facility, Karl-Schwarzschild-Straße 2, D-8046, Garching bei München, Germany
PETER G. MARTIN
Canadian Institute for Theoretical Astrophysics, 60 St. George Street, Toronto, Ontario, Canada M5S 1A1
AND
GLADIS MAGRIS C.
Centro de Investigaciones de Astronomia (CIDA), Apartado Postal 264, Mérida 5101-A, Venezuela
Received 1993 January 19; accepted 1993 March 22

ABSTRACT

We present detailed calculations on the effects of internal dust on the Balmer and Lyman decrements for a spherically symmetric distribution of low covering factor clouds photoionized by a power law. In the first stage, we assume an open geometry with clouds represented as slabs and consider the effects of Lyα resonance and absorption by dust. We consider the important effects of perspective on the emergent fluxes, which in our simplified scheme present either the photoionized face to the observer ("f") or the back ("b") face. We adopt canonical values for the gas excitation (U_f) and for the ionizing energy distribution ($\alpha = -1.4$, $F_\nu \propto \nu^{+\alpha}$). After reviewing the effects of separately varying the gas density in the dust-free case, we adopt a single representative density of 5000 cm^{-3} in all our calculations and proceed to compute sequences of photoionization models in which the relative internal dust content by mass (μ) is progressively increased to values comparable to the local ISM (i.e., $\mu = 1$). Although we always adopt solar metallicity for the gas+dust phases, as we increase μ we deplete the gas phase abundances in accordance with current knowledge of the depletion indices following a procedure described in Appendix A. We find that for moderate amounts of internal dust $\mu = 0.2$–0.3, radiation-bounded clouds result in Lyman and Balmer decrements in the range 32–37 and 3.0–3.1, respectively. To cover the case in which the clouds are more massive than implied by the condition of being radiation-bounded, we also consider adding a neutral gas+dust zone of column density $N^0_{\rm H^0}$ beyond the partially ionized zone. Our main result, valid for the calculations with standard NLR input parameters and for an open geometry in which multiple cloud covering is negligible, is that even with internal dust, while Hα/Hβ is reddened, Lyα/Hβ turns out not very different from recombination case B. The Seyfert 2 observations show much lower Lyman decrements than predicted from the spherically symmetric model and a critical study is made of various explanations: dust- or line-scattering screens, a semiopen geometry or a fully closed spherical geometry. We find that Lyα/Hβ and Hα/Hβ obtained from calculations using a semiopen geometry can span the region covered by the Seyfert 2 observations. We also study the possibility that dust reddening of the *continuum* may account for the apparent deficit of ionizing photons seen in many Seyfert 2's. This reddening may be present in addition to, or in place of, the anisotropic beaming/occultation of ionized radiation (cf. "occultation/reflection picture") that is generally invoked to explain the deficit.

Subject headings: dust, extinction — galaxies: Seyfert — radiative transfer

1. INTRODUCTION

The calculation of the intrinsic Balmer decrement emitted by the narrow-line region (NLR) of Seyferts has attracted much interest in the past (e.g., Gaskell 1984; Malkan 1983; Halpern & Steiner 1983; and Ferland & Netzer 1983) because it is the most direct means of determining how much (intervening) extinction the observed emission-line spectrum has undergone. This information can be used to deredden the whole line spectrum for the effect of external dust along the line of sight. It has been recognized early on by Halpern & Steiner (1983) and Ferland & Netzer (1983) that the NLR intrinsic Balmer decrement was likely to be higher than that of recombination case B as a result of collisional excitation within the partially ionized zone. The resolution of the problem of intrinsic H I line ratios was further advanced by combining the information provided by the Lyman decrement with that of the Balmer decrement (e.g., Ferland & Osterbrock 1985). Gaskell & Ferland (1984) studied in details how the NLR metallicity, density, and hardness of the ionizing continuum affected both decrements. The most probable range for the NLR decrements which these authors favor is Hα/Hβ = 2.8–3.1 and Lyα/Hβ = 30–50 (similar to values determined earlier by Ferland & Osterbrock 1985). The observational determination of the intrinsic H I line ratios is facilitated in Seyfert 2 galaxies since one need not decompose the line profiles into BLR and NLR components. However, Seyfert 2's are on average significantly more reddened than Seyfert 1's (Gaskell 1984). De Zotti & Gaskell (1985) concluded that the dust was probably associated with the NLR clouds or filaments owing to the extremely weak correlation of the extinction with disk inclination angle and

[1] Also visiting the Space Telescope—European Coordinating Facility.

also due to the significantly lower extinction found in Seyfert 1.5.

If there is so much dust associated with the nuclear emission region, we might expect some dust to be associated with the photoionized gas itself. The effect of internal dust mixed with ionized gas for physical conditions pertaining to the broad-line region (BLR) has been investigated by Ferland & Netzer (1979). More recently, however, Netzer (1993) concluded that the BLR was devoid of dust (but see Crosas 1993). From considering the ratios Hα/Hβ *vs.* Hγ/Hβ in Seyfert 2's, Binette et al. (1990) suggested the possibility of an intrinsic (NLR) Balmer decrement as high as Hα/H$\beta \approx 3.4$, which they modeled using photoionization calculations with dust internally mixed with the ionized gas.

Internal dust results not only in somewhat higher Balmer decrements but can furthermore increase the equilibrium temperature of the ionized gas. This property was used by Magris, Binette, & Martin (1993) to solve the problem of the high electronic temperature (based on [O III] lines) observed in the extended ionized nebulosities of powerful radio galaxies (cf. Tadhunter, Robinson, & Morganti 1989). Furthermore, dust can reflect towards the observer a nonnegligible fraction of the impinging optical radiation, an interesting property which appears to explain quite well the extended blue polarized continuum observed in distant radio galaxies (cf. Fosbury 1993; Cimatti et al. 1993; Binette et al. 1993a). Dust may also explain the absence of any intermediate region between the BLR and the NLR according to Netzer & Laor (1993), not to mention its relation with the infrared emission (Clavel, Wamsteker, & Glass 1989; Barvainis 1992; Sanders et al. 1989; Pier & Krolik 1992).

In this work, we expand upon the calculations of Binette et al. (1990) and study the effects of internal dust on the intrinsic Hα/Hβ by taking into account the observer's perspective of the emitting clouds. In addition, we consider the effect of dust on the Lyman decrement. Kwan & Krolik (1981) and Puetter & Hubbard (1987) have shown using dust-free BLR calculations how significant is the effect of perspective on resonant Lyα. With dust mixed in, it becomes essential to take into account satisfactorily the cloud's perspective and the global NLR geometry when deriving the intrinsic decrements, as described in § 2. We first investigate in § 3 the magnitude of the Lyα destruction due to internal dust in photoionization calculations and compare in § 4 our calculations with the Seyfert 2 data Kinney et al. (1991).

2. COMPUTATIONAL METHOD

We describe the photoionization code and the line transfer of Lyα, Hα, and Hβ across the dusty medium and review the input parameters that enter our calculations.

2.1. *The Photoionization Code*

To compute H I lines we have employed the multipurpose photoionization-shock code MAPPINGS (cf. Binette, Dopita, & Tuohy 1985). To compute the hydrogen lines, we treat the hydrogen atom as a six-level system (1*s*, 2*s*, 2*p*, 3, 4, and 5) plus continuum. The hydrogen levels are populated through direct recombination (followed by cascade) as well as by collisional excitation either by thermal electrons (using Johnson 1972 rate coefficients) or by suprathermal electrons (adopting the method developed by Shull & Van Steenberg 1985) as earlier described in Binette et al. (1983b, hereafter BWZM).

In the computation of the ionization structure, we adopt a simple plane-parallel geometry whereby our putative thick gas cloud is represented by a radiation-bounded slab of gas containing interstellar dust. The ionized slab is subdivided into many small layers in which the equations of photoionization and thermal equilibrium are solved by standard methods.

The escape probability formalism is used to solve for the transfer of the resonance lines. The effects of dust on the ionization structure as well as on the thermal balance of the plasma are considered in detail by implementing the physical processes relevant to dust mixed with emission plasma as described in Appendix C of Baldwin et al. (1991). For instance, heating of the plasma by dust photoelectric emission is considered. The dust grain charge is calculated self-consistently and the formula describing the photoelectron energy distribution and the yield are from Draine (1978), but with a cap of 0.2 for the yield at high photon energies as in Baldwin et al. (1991).

One interesting aspect of the new code MAPPINGS is that the effect of dust scattering on the line transfer is explicitly solved using the numerical solution of Bruzual, Magris, & Calvet (1988). This aspect of the transfer is particularly relevant to the "open geometry" adopted for most of the calculations presented in this paper. Destruction of the resonant lines by dust absorption is taken into account using the results of Hummer & Kunasz (1980). We describe in more details in Appendix A of BWZM the method implemented in MAPPINGS for solving the line transfer of emission plasma with internally mixed dust.

2.2. *Trace Elements and Dust Content*

Even though this paper only addresses the intensities of hydrogen lines, the abundance of trace elements remains an important factor since they affect directly the thermal balance of the photoionized plasma. Abundance gradients observed in spiral galaxies point towards a metallicity even higher than solar for the nuclear region. Many models of the NLR on the other hand have favored more often than not the exploration of abundances lower than or equal to solar (e.g., Gaskell & Ferland 1984; Ferland & Netzer 1983). As the current work emphasizes the rôle of internal dust, for definiteness we will assume that the abundances of metals appropriate to the NLR are close to solar and adopt the solar system abundances of Anders & Grevesse (1989) (see list in Table A1 of Appendix A). We define Z as the total (gas + dust phases) metallicity relative to solar which implies $Z \equiv 1$ for this work.

The absorption and scattering cross sections of dust (from the infrared to the soft X-rays) were computed by one of us (P. M.) (the curves are displayed in Fig. 6 of Martin & Rouleau 1991) and corresponds to a dust model of the extinction curve of the solar neighborhood interstellar medium. In MAPPINGS, we scale the scattering and absorption cross sections (and, therefore, the dust content) by a dimensionless factor μ. The grain model of Martin & Rouleau (1991) results in a dust-to-gas *mass* ratio of 0.0064 μ ($\rho_{\rm dust}/\rho_{\rm gas} \cong 0.71\rho_{\rm dust}/\rho_{\rm H}$) and to an extinction opacity at 5500 Å τ_V ($= 0.921 A_V$) $= 4.8 \times 10^{-22}\ \mu\ N_{\rm H}\,{\rm cm}^2$, where $N_{\rm H}({\rm cm}^{-2})$ is the *total* hydrogen column density. When $\mu \equiv 1$, these quantities are all consistent with the standard extinction curve of the local ISM (interstellar medium).

To be consistent with the depletion of metals unto dust grains, we deplete the abundance of metals in the *gas* phase, $Z_{\rm gas}$, according to the dust content μ. The adopted scheme described in Appendix A uses the depletion indices listed in Whittet (1992) and if necessary scales them with μ/Z. Re-

normalization of the derived gas phase abundances is performed until the mass locked into dust grains becomes consistent with the dust-to-gas mass ratio implied by μ. For instance, when $\mu = 1$, $Z_{\rm gas} = 0.6$ as a result of depletion. In this work, the *total* metal abundances are always solar and, therefore, $Z = Z_{\rm gas} + Z_{\rm dust} \equiv 1$.

2.3. *The Slab Geometry and the Input Parameters*

All our calculations assume the same standard values for the input parameters, that is: an isobaric density behavior, a power law ionizing continuum of index $\alpha = -1.4$ ($F_\nu \propto \nu^{+\alpha}$) and solar *total* abundances (but depleted gas abundances: $Z_{\rm gas} = Z - Z_{\rm dust} = 1 - Z_{\rm dust}$). Our constant pressure models are parameterized in terms of the so-called ionization parameter, that is, the ratio of the density of ionizing photons impinging on the slab to the density of the outermost gas layer of the slab:

$$U_f = \frac{1}{cn_{\rm H}^f}\int_{\nu_0}^{\infty}\frac{\varphi_\nu^f}{h\nu}\,d\nu = \frac{\varphi_{\rm H}^f}{cn_{\rm H}^f}\,, \qquad (1)$$

where c is the speed of light and ν_0 is the Lyman limit frequency, $\varphi_{\rm H}^f$ is the ionizing photon flux (in photons cm^{-2} s^{-1}) impinging on the slab. (Quantities with superscripts f or b refer to their values at the front or at the back of the slab, respectively). For the reference dust-free model (*filled star* in the figures) which is referred below, we adopted $n_{\rm H}^f = 5000$ cm^{-3} cm^{-3} and $U_f = 0.0015$ as justified in §§ 3.1 and 3.3.

Using the code MAPPINGS, the calculation of the ionization and emissivity structure is carried inward in the slab either up to a column depth (i.e., $\int n_{\rm H}\,dx$) $N_{\rm H}^{\rm slab} < N_{\rm H^*}$ in the case of matter-bounded calculations or, in the case of radiation-bounded calculations, up to $N_{\rm H^*}$. The column density $N_{\rm H^*}$ gives the depth of the complete "photoexcited" region, that is, the depth at which the incoming ionizing flux is exhausted. The operative definition of the boundary of the photoexcited region (at depth $N_{\rm H^*}$) is defined as the depth where the following two conditions are simultaneously satisfied: (1) the inabsorbed ionizing flux $\varphi_{\rm H}^b(N_{\rm H^*}) < 1\%$ of the impinging flux $\varphi_{\rm H}^f$, and (2) the ionized fraction $n_{\rm H^+}^b/n_{\rm H}^b \leq 1\%$. The code computes successively the emergent flux seen directly from the photoionized face (perspective "f"; see Fig. 1) as well as seen from the back (perspective "b"). The transfer solution used across the dusty medium not only considers absorption but dust scattering as well (see BWZM).

Because the harder photons of the power-law ionizing continuum (with $\alpha = -1.4$) creates quite a large partially ionized region (hereafter PIZ) in which the ionized gas very gradually becomes neutral, $N_{\rm H^*}$ is a factor ~ 10 higher than the Strömgren depth (in cm^{-2}) which is technically defined as

$$N_{\rm H^+}^S = cU_f/\alpha_B \approx 10^{23}U_f\ {\rm cm}^{-2}\ (T_e = 10^4\ {\rm K})\,, \qquad (2)$$

where α_B is the recombination coefficient to excited states of hydrogen. In an H II region, because of the softness of the ionizing continuum, the PIZ is negligible and $N_{\rm H^*} \cong N_{\rm H^+}^S$. For a power-law ionizing continuum, $N_{\rm H^*} \gg N_{\rm H^+}^S$, although $N_{\rm H^+}^S$ traces well the column density of ionized gas of the whole slab ($N_{\rm H^+}^{\rm slab} \cong N_{\rm H^+}^S$). For radiation-bounded clouds, equation (2) entails that the fully ionized zone [$N_{\rm H^+}(n_{\rm H^+}/n_{\rm H^0} \geq 10) \approx 0.8N_{\rm H^+}^S$] which contributes most of the line luminosity nevertheless contributes only a small fraction of the dust opacity inside $N_{\rm H^*}$ and, therefore, the spectrum seen from perspective "b" is more reddened than the one emerging from perspective "f."

By portraying the emitting NLR cloud as a slab, a determinant parameter with which the dust opacity scales is the total column density $N_{\rm H}^{\rm slab}$ ($= N_{\rm H^+}^{\rm slab} + N_{\rm H^0}^{\rm slab}$) of the slab. In this work, in most instances, we assume the slab to be not only radiation-bounded but in some cases to exceed $N_{\rm H^*}$ due to a neutral H^0 zone of column density $N_{\rm H^0}^0$ (beyond the PIZ) as depicted in Figure 1. The dust inside this region can play a determinant role in reducing the emergent line fluxes seen from perspective "b." Apart from absorption of the lines by dust, the neutral zone also reflects toward the front the small fraction of resonant Lyα which would otherwise emerge from perspective "b." This neutral zone is assumed isothermal with a temperature taken to be equal to the temperature at the last computed ionized layer. Changing this temperature even arbitrarily has practically no effect on the zone's reflectivity to Lyα since even without such a zone the already huge Lyα line opacity within the PIZ would cause most of the Lyα to emerge from perspective "f" rather than from "b" (cf. 3.2).

In our nomenclature, the total column density of the slab is given by $N_{\rm H}^{\rm slab} = N_{\rm H^*} + N_{\rm H^0}^0$ (see Fig. 1) if the slab is radiation-bounded (otherwise, $N_{\rm H}^{\rm slab} < N_{\rm H^*}$ if the slab is matter-bounded). We assume that the dust-to-gas ratio μ is uniform within each zone but may take different values in the photoexcited zone from that in the neutral zone. Assuming that the same dust size distribution and composition applies to the different zones (that is, the shape of the extinction curve remains constant), we obtain that the total slab opacity in the V band (5500 Å) is given by

$$\tau_V^{\rm slab} = \tau_V(N_{\rm H^*}) + \tau_V(N_{\rm H^0}^0) = 4.8 \times 10^{-22}[\mu({\rm H^*})N_{\rm H^*} + \mu({\rm H^0})N_{\rm H^0}^0]\,. \qquad (3)$$

Due to the high reflectivity of Lyα by the H^0 zone as well as by the substantial amount of H^0 inside the transition zone, the emergent Lyα originating from perspective "b" is generally negligible. The Balmer lines are generated isotropically but are absorbed differently when emerging from perspective "b" or "f" because of the asymmetry in dust opacity introduced by the $N_{\rm H^0}^0$ zone and the PIZ. If we picture the NLR as an ensemble of clouds with very low covering factor symmetrically distributed around a nuclear ionizing source, the *number* of clouds

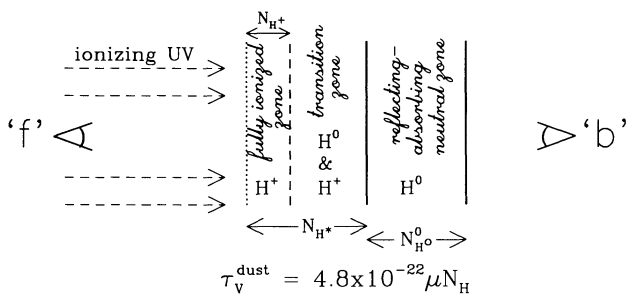

FIG. 1.—Adopted slab geometry for the constant pressure photoionization calculations. The slab comprises a fully ionized zone and a partially ionized zone (PIZ) which adds up to the column density of the photoexcited zone $N_{\rm H^*}$. Beyond the PIZ, we may have a zone of neutral gas of column density $N_{\rm H^0}^0$. The total depth of the slab is $N_{\rm H}^{\rm slab} = N_{\rm H^*} + N_{\rm H^0}^0$. The total hydrogen gas density $n_{\rm H}^f$ and the impinging ionizing flux $\varphi_{\rm H}^f$ on the ionized side defines the ionization parameter U_f (see eq. [1]). Perspective "f" considers the emergent line fluxes seen from the side which is photoionized (front), while perspective "b" corresponds to the opposite back side. The dust extinction opacity of any zone is proportional to its relative dust content μ and total hydrogen column density $N_{\rm H}$.

seen from the back can be postulated to be equal statistically to that of clouds seen from the front. To a first order the resulting line ratios for such an "open" geometry is obtained by adding first with equal weight the line fluxes from the "f" and "b" perspectives and then taking the ratios of the summed fluxes.

In § 3, we will first explore the effect of varying the internal dust-to-gas ratio μ on the Lyα/Hβ and Hα/Hβ line ratios emerging from a symmetric distribution of clouds (i.e., the case represented by "f" + "b"). After comparing models (§ 4.1) with the Seyfert 2 data of Kinney et al. (1991, KAW3) and after discussing the pure dust hypothesis (§ 4.2), we will look into the possibility of having more clouds seen from perspective "b" as well as the limiting case of a spherically closed geometry (§ 4.3).

3. RESULTS

Our main purpose is to explore the effect of internal dust on the H I line ratios in the context of the standard photoionization model of the NLR. For this reason, we have limited the scope of the calculations to restricted plausible values of the input parameters; we consider, for instance only solar abundances (but with progressive depletion of gas phase metallicity $Z_{\rm gas}$ with increasing dust content μ) and a canonical $\alpha = -1.4$ ionizing power law[2] (cf. Ferland & Osterbrock 1986; Kinney et al. 1991). The choice and role of the gas density is first discussed (§ 3.1) as well as that of incomplete opacity to ionizing photons (§ 3.2) and the selection of the ionization parameter (§ 3.3). We then discuss the results of nebular models with internal dust in § 3.4.

3.1. *Selection of a Characteristic Cloud Density*

The choice of a representative cloud density in the calculations is much more problematic than the selection of other parameters. There is evidence of a wide distribution of cloud densities in the NLR following the work of DeRobertis & Osterbrock (1984, 1986) who have shown in many Seyferts the tendency of the forbidden line profile widths to correlate with the respective deexcitation critical density of the transition involved. This lends support to the picture of a wide gradient in cloud densities ($10^3 \leq n_e \leq 10^6$ cm^{-3}) as well as in velocity dispersion as a function of distance from the nucleus. In this picture, the bulk of a line luminosity would be contributed by clouds of density approaching the line's critical density. The few available direct measurement of the NLR electron densities have been mostly provided by the ratio of the [S II] λ6716/λ6731 density-sensitive doublet (Osterbrock 1989) which show densities which are relatively low (200–2000 cm^{-3}). These low densities do not necessarily contradict a wide range of cloud densities within the NLR because the critical density of [S II] red lines is relatively low and moreover the S^+ zone coincides with the partially ionized zone of the emitting cloud where the electron density can be expected to be lower than in the fully ionized zone. This can be demonstrated with constant pressure photoionization calculations with densities covering the range $80 < n_{\rm H}^f < 6000$ cm^{-3} which show that the electronic density inferred from the [S II] line ratio is a factor 4–5 smaller than the mean $\langle n_e \rangle$ of the fully ionized zone. Finally, there also exists a significant fraction of Seyferts in which line widths correlate with line excitation (cf. Pelat, Alloin, & Fosbury 1981; Filippenko 1985; DeRobertis & Osterbrock 1984, 1986) which could indicate that the density range within these objects is narrower.

Following the indications given by the [S II] densities and given that we will not integrate the line contribution of clouds over different densities, we opt for a single density of $n_{\rm H}^f = 5000$ cm^{-3} which we expect to characterize the NLR gas that emits the bulk of the H I lines. Before discussing models with dust, we first summarize the dependence of H I lines on density.

The direct dependence of Hα and Hβ intensities on the gas density is very weak when the line is produced by recombination alone (Hummer & Storey 1987). However, in a power-law photoionized plasma, both lines become indirectly coupled to density when substantial collisional excitation takes place within the PIZ. The reason is that increasing the density reduces the effectiveness of cooling of many important forbidden lines as a result of collisional deexcitation, thereby increasing the equilibrium plasma temperature which in turn increases the rate of collisional excitation of H I in the PIZ. In the fully ionized zone, there is too little H I to excite and the Balmer lines are produced only by recombination independent of the plasma temperature. In the case of Lyα, the dependence of the line intensity on the electron density is much more direct. When the density is increased much above 10^3 cm^{-3}, there is an increasing conversion of the level $2s$ population otherwise responsible for the $2q$ continuum emission into Lyα emission by excitation into the $2p$ level (see Osterbrock 1989; Gaskell & Ferland 1984). In the low density regime case B in the absence of Lyα sinks (e.g., dust absorption), the fraction of energy emitted as Lyα versus $2q$ emission from recombination alone is $\alpha_{2p}^{\rm eff}/\alpha_B \approx 0.67\,(T_e/10^4\ {\rm K})^{-0.054}$ and tends toward unity for densities above 10^5 cm^{-3}.

To illustrate quantitatively the effect of density, we have calculated a sequence of constant pressure models covering the range $50 \leq n_{\rm H}^f \leq 2 \times 10^6$ cm^{-3}. The results of integrated nebulae calculations as a function of the mean slab electron density are presented in Figure 2. The case of a pure recombination-dominated H II region model (*dotted line*) is also shown for comparison with the power-law model (*solid line*). In Figure 2*a*, it is evident that both ionizing energy distributions result in a qualitatively similar functional dependence of Lyα/Hβ on $\langle n_e \rangle$, except that Lyα/Hβ is consistently higher for the power law due to collisional excitation within the PIZ. For the Balmer decrement (Fig. 2*b*), at low densities ($\langle n_e \rangle \ll 5 \times 10^4$ cm^{-3}) it likewise is somewhat higher for the power law. At high densities ($\langle n_e \rangle > 5 \times 10^4$ cm^{-3}), however, there is a sharp increase in Hα/Hβ owing to the enhancement of collisional excitation that occurs when the gas temperature increases due to gradual suppression of the forbidden lines.

Subsequent models with internal dust have all been calculated with the single representative density of $n_{\rm H}^f = 5000$ cm^{-3}. This reference density coupled with the adopted U_f introduced below provides us with a comparative zero point (i.e., dust-free case) in our Lyα/Hβ versus Hα/Hβ diagrams (as represented by the filled star). If one is interested in estimating the line ratios from the results presented below with internal dust but for a different zero point in density space, Figure 2 can be used to determine very approximately the differential change in the ratios due to density alone and apply it to the models which contain dust.

3.2. *Asymmetric Emissivity and Internal Dust Absorption*

Because line scattering increases the path length of Lyα photons, the efficiency of internal dust to absorb line photons

[2] A much harder energy distribution (flatter power law) would give a rather poor fit to the low excitation lines assuming the photoionized clouds are radiation bounded.

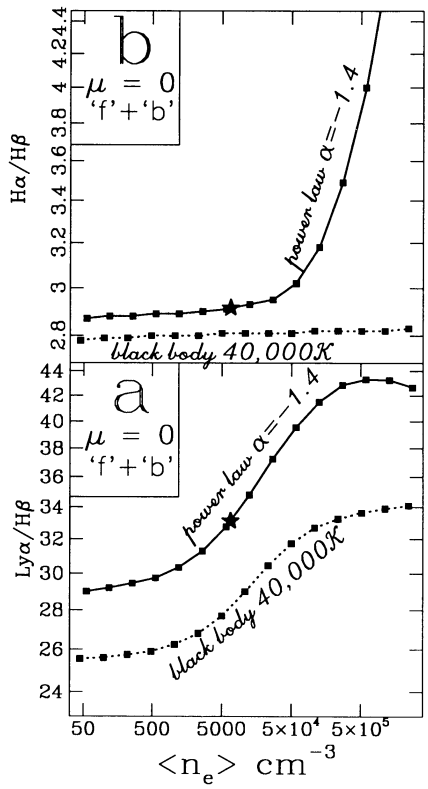

FIG. 2.—Sequences of dust-free solar metallicity photoionization calculations with varying gas density n_H^f. Results for two different energy distributions of the ionizing continuum are represented: the power law with $\alpha = -1.4$ (*solid line*) adopted in this work and a blackbody of 40,000 K (*dotted line*) for which recombination is the only process generating the H I lines. The ionization parameter U_f is constant along both sequences and takes on the values of 0.0015 and 0.010 for the power law and for the blackbody sequences, respectively. Panel (*a*) shows the Lyα/Hβ ratio ("f" + "b") as a function of the mean electron density $\langle n_e \rangle$ characterizing the isobaric photoexcited zone, while panel (*b*) shows the corresponding behavior of Hα/Hβ. The star represents the standard model ($U_f = 0.0015$, $n_H^f = 5000\ \mathrm{cm}^{-3}$) discussed in § 3.

is drastically higher for the optically thick resonant Lyα line than for the optically thin Balmer lines. Hummer & Kunasz (1980) have derived scaling laws for the energy loss, the mean path length, and the mean number of scatterings suffered by resonant line photons in the presence of continuous absorption (by dust and/or photoelectric absorption). (See Neufeld 1990 for a discussion of these scaling laws using analytical methods.) The fraction of energy from a resonant line generated within a midplane layer which escapes unabsorbed from a slab of total line opacity Γ depends essentially on the parameter $\beta \equiv k_c/k_L$ which is the ratio of continuous opacity to line opacity. The results of Hummer & Kunasz (1980) concerning the transfer as well as the interplay between escape probability and dust absorption have been incorporated in MAPPINGS as described in detail in Appendix A of BWZM.

One aspect of the transfer particularly relevant to thick nebulae is the asymmetry which characterizes the Lyα flux emerging from the front or from the back of the ionized slab. This is taken into account in the code through the definition of an emissivity whose asymmetry depends on the local two-sided escape probability. The asymmetry factor $A^f (0 \leq A^f \leq 2)$ in our transfer solution is defined as follows

$$A^f = 2\epsilon(\tau, \beta)/[\epsilon(\tau, \beta) + \epsilon(\Gamma - \tau, \beta')] , \quad (4)$$

where τ is line opacity of the layer under consideration, Γ ($= \int d\tau$) is the line opacity of the whole slab, $\epsilon(\tau, \beta)$ is the escape probability from the front, and $\epsilon(\Gamma - \tau, \beta')$ is the escape probability from the back. (See Appendix A in BWZM for further details on the escape asymmetry.) The implication of the two-sided escape scheme is that the emissivity of the resonant line is asymmetric with the forward emissivity given by $j_L^f = j_L A^f$ and the back emissivity by $j_L^b = j_L(2 - A^f)$. The observer, in this simple two-stream transfer scheme, is placed either in front of the slab or behind it and the emergent line flux from either perspective "f" or "b" is obtained by integrating the appropriate emissivity (j_L^f or j_L^b).

An important consequence of using equation (4) in integrating the line emissivity is that for a slab illuminated on only one side by the ionizing radiation, the Lyα intensity emerging from perspective "f" is much higher than that from "b" whenever the line is reasonably thick ($\tau > 10$), a condition almost always satisfied except for extremely low column density matter-bounded slabs. For a slab of total line opacity Γ, the depth N_H at which line photons have equal probability of escaping from the front ("f") as from the back ("b") occurs at the depth for which $\tau = \Gamma/2$, i.e., $N_H = N_H(\tau = \Gamma/2)$. Since $d\tau/dN_H \propto n_{H^0}/n_H$ is a monotonically increasing function of N_H, the depth $N_H(\tau = \Gamma/2)$ is quite generally located much deeper than the depth that divides equal Lyα production. As a result, Lyα photons preferentially escapes from the front ("f"). This is true even for soft impinging ionizing continua as occurs, for instance, in H II regions. For a power-law ionizing continuum, to the extent that recombination still dominates Lyα production, most of the Lyα is produced within the fully ionized zone, i.e., at $N_H \lesssim 0.8 N_{H^+}^S$ which is much less than $N_H(\tau = \Gamma/2) \sim N_{H^*}$ owing to the extended PIZ (cf. § 2.3). In the opposite case of extremely low column density nebulae, the neutral fraction $n_{H^0}/n_H \approx$ constant so that $N_H(\tau = \Gamma/2) \approx N_H^{slab}/2$, which coincides approximately with the depth dividing equal Lyα production. In this case, the Lyα flux emerges symmetrically from the front ("f") and back ("b").

To illustrate how one progressively goes from symmetrically emerging Lyα in the very thin slab case to the opposite asymmetric situation in the radiation-bounded slab case, we have computed a sequence of matter-bounded models in which N_H^{slab} is gradually increased in lock steps. Figure 3 gives the fraction of Lyα which escapes from perspective "b" as a function of the matter-bounded slab's thickness (expressed in a different way in each panel). Note that internal dust has been included in these models, but it does not affect significantly the degree of asymmetry except when N_H^{slab} approaches N_{H^*}, the radiation-bounded case. Two of the sequences correspond to $U_f = 0.0015$ with internal dust set at either $\mu = 0.2$ or 1.0, and one sequence represents a higher ionization parameter $U_f = 0.015$ with $\mu = 1.0$. The results indicate that the fraction of Lyα which escapes from the back is close to half only when the matter-bounded slab is indeed very thin (i.e., for $\tau_{H^0}^c(912\ \text{Å}) < 10$ or $N_H^{slab}/N_{H^+}^S < 0.5$–0.8).

The effect of perspective need not be considered in previous work on the intrinsic NLR Lyα/Hβ and Hα/Hβ line ratios since it was implicitly assumed that perspective effects averaged out due to the geometry of the ensemble of NLR clouds. This might be a valid assumption in the dust-free case where no Lyα destruction takes place despite the high number of scatterings. When dust is present, however, the effect of perspective cannot be ignored since the Lyα transfer with internal dust present is nonconservative with respect to perspective

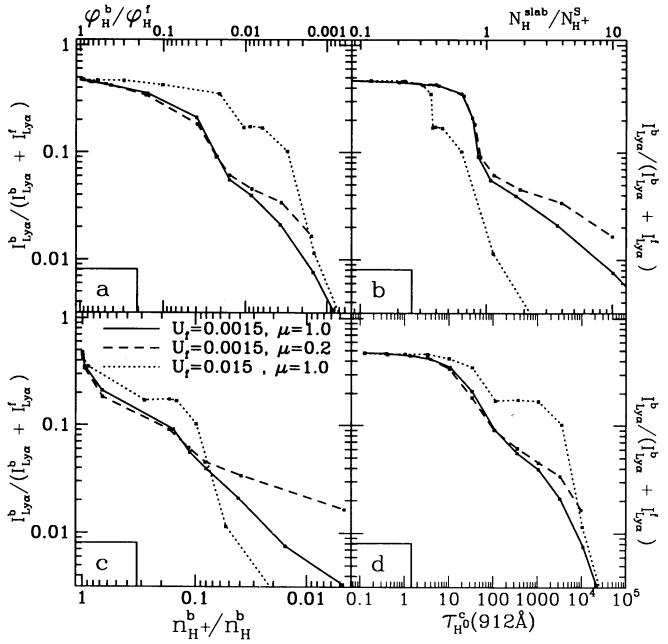

FIG. 3.—Matter-bounded calculations in which the ordinate represents the fraction of Lyα flux which escapes from the back (perspective "b") as a function of different quantities which measures the ionized slab's thickness. The abscissae represent, panel for panel, the following: panel (*a*): the fraction of unabsorbed ionizing photons which leaks out from the back φ^b_H/φ^f_H; panel (*b*): the slab's column density to that of the Strömgren depth $N^S_{H^+} = cU_f/\bar{\alpha}_B$, where $\bar{\alpha}_B$ is evaluated at the slab *mean* electronic temperature; panel (*c*): the hydrogen ionized fraction within the last layer at the back; panel (*d*): the slab Lyman-limit continuum opacity. The solid and short dash curves were both calculated using the reference value of $U_f = 0.0015$ (and $n_{Hf} = 5000$ cm^{-3}; see §§ 3.2 and 3.3) but with an internal dust content of $\mu = 1.0$ and 0.2, respectively. The dotted line corresponds to calculations with $U_f = 0.015$ and $\mu = 1.0$.

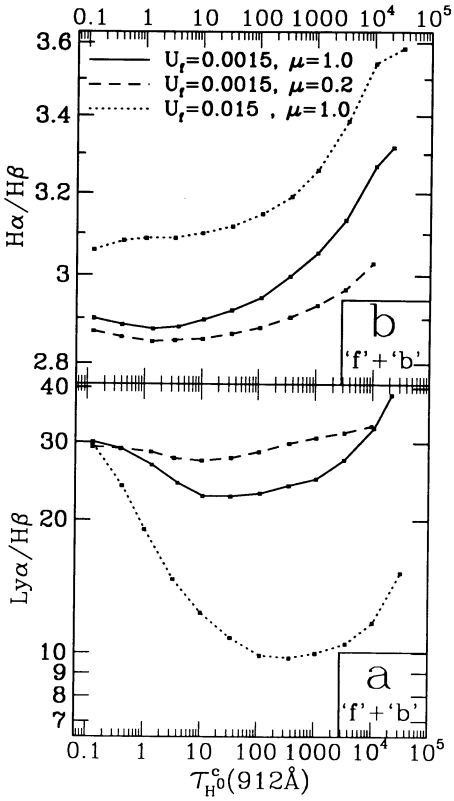

FIG. 4.—In panel (*a*), Lyα/Hβ as a function of the Lyman-limit opacity of the matter-bounded photoionized slabs. As in Fig. 3, the solid and short dash curves were calculated with $U_f = 0.0015$ and an internal dust content of $\mu = 1.0$ and 0.2, respectively. The dotted line corresponds to calculations with $U_f = 0.015$ and $\mu = 1.0$. Panel (*b*) plots the Balmer decrement as a function of the Lyman-limit opacity.

with most of the surviving Lyα photons escaping from the front.

Perspective can also affect significantly the integrated Balmer lines of a system of clouds with internal dust because the dust within the extensive PIZ significantly absorbs the Balmer lines which emerges from the back (producing at the same time a steeper Balmer decrement). This effect is particularly important in understanding the results presented in § 3.4. To illustrate the dominant effects of both perpective and dust, we picture a thin fully ionized region which generates the bulk of Lyα, and, depending on how opaque the region is to dust [$\tau_V(H^+)$], a substantial fraction of the resonant Lyα escapes from the front while half of the Balmer lines' flux is required to transfer across the larger and dustier PIZ before escaping from the back (the other half emerges from the front after suffering little extinction).

To illustrate the role of internal dust on the total emerging Lyα and Balmer lines, we present in Figure 4 the line ratios resulting from adding together the fluxes from perspective "f" and "b" (before taking the ratio) as a function of the Lyman limit opacity $\tau^c_{H^0}$(912 Å) for the matter-bounded sequences presented in Figure 3. The larger destruction rate of Lyα for the high-ionization parameter (*dotted line*) model is apparent and is the result of a higher value of β throughout the nebula (cf. § 3.3). We also find for all three sequences that for $\tau^c_{H^0}$(912 Å) > 100, because dust in the PIZ starts absorbing much of the Hβ flux escaping from the back, the "f" + "b" Lyα/Hβ ratio rebounds up (the Lyα flux actually remains steady). The somewhat higher Balmer decrement in the matter-bounded regime in the higher U_f model is generally caused by reddening [larger $\tau_V(H^+)$]. When $\tau^c_{H^0}$(912 Å) < 10, then, in addition to reddening, for β sufficiently high, the normal conversion of the higher Lyman lines into Balmer or higher series is reduced because of dust absorption of these Lyman lines (this effect simulates something resembling case A).

3.3. *Selection of the Ionization Parameter U_f*

The most simple geometrical model of the narrow-line region consists of a symmetric distribution of ionized clouds surrounding the ionizing source. Any reasonably assumed electron densities leads us to infer a very small *volume* filling factor for the emitting gas. The ionization parameter which is inferred from the line ratios is surprisingly uniform within a given class of AGN.

To determine U_f, we have simply required the radiation-bounded calculations to approximately fit the "mean" optical Seyfert 2 line spectrum derived by Ferland & Osterbrock (1986, hereafter FO86) in which a ratio of [O III] λ5007/Hβ of ~10 is observed. With the other parameters specified above, this leads us to adopt $U_f = 0.0015$ for the reference ionization parameter.

The choice of the ionization parameter affects strongly the role played by dust. For instance, internal dust can absorb a fraction of the ionizing radiation and therefore shrink the Strömgren depth due to competitive absorption with H^0. In the case of our reference model with $U_f = 0.0015$, only 3% of

φ^f_H is lost to dust absorption when $\mu = 1$. However, with an ionization parameter 10 times larger [recall that $\tau_V(H^+)$ scales with $N^S_{H^+}$], we find that as much as 24% of φ^f_H is absorbed by dust when $\mu = 1$. This effect can be seen in $U_f = 0.015$ sequence shown in Figure 3*b* where the dotted line curve is shifted to the left because the scaling is relative to the dust-free value of $N^S_{H^+}$.

Another aspect where U_f is important is the amount of destruction of resonant Lyα by dust. To show this, let us define using equation (2) the pure absorption opacity by dust at a depth halfway within the fully ionized zone:

$$\tau^{abs}_{dust}(1216\ \text{Å}, \tfrac{1}{2}N^S_{H^+}) \cong 2.2\tau^{ext}_V \approx 60\mu U_f\ . \quad (5)$$

The justification for choosing this position is that most of the Lyα is generated as well as destroyed within the fully ionized region. Assuming $U_f = 0.0015$ and $\mu = 1.0$, we obtain $\tau^{abs}_{dust}(1216\ \text{Å}) \approx 0.1$. As a crude estimate to illustrate the effect of dust on Lyα, at this depth, the line (scattering) opacity is $\sim 10^5$ which allows us to estimate $\beta \sim 10^{-6}$ and derive the fraction of Lyα which escapes unabsorbed from this layer at $\sim 50\%$ by using the scaled results of Hummer & Kunasz (1980). On the other hand, for the higher value of $U_f = 0.015$, the line opacity at a similar relative position corresponding to $\tau^{abs}_{dust}(1216\ \text{Å}) \approx 1$ ($\mu = 1$) is higher ($\sim 3 \times 10^6$), and we estimate that with $\beta \sim 3 \times 10^{-7}$, only 2% of Ly$\alpha$ escapes the layer. For calculations with the adopted ionization parameter $U_f = 0.0015$, we see that Lyα destruction due to dust should be moderate.

3.4. *Results for a Symmetric Cloud Distribution*

We approximate the typical NLR emission cloud as a slab of gas of constant internal pressure with an outer density of $n^f_H = 5000\ \text{cm}^{-3}$ (cf. § 3.1). Using MAPPINGS, we compute the line spectrum from photoionization calculations using the ionization parameter $U_f = 0.0015$ (cf. § 3.3) and an ionizing power-law of index $\alpha = -1.4$. In all the calculations, the gas phase abundances is modified consistently with the dust content μ in such a way that the total metallicity (gas + dust) remains always solar: $Z = Z_{gas} + Z_{dust} = 1$ (cf. § 2.2 and Appendix A). The assumed symmetric distribution of the clouds is taken into account in the calculated spectrum by adding together spectral "f" and "b" of MAPPINGS' calculations which is equivalent to supposing that there are as many clouds seen face-on as are seen from the back.

Using this procedure, we have computed three sequences of models with the dust content μ to covering the range $0 \le \mu \le 1.25$. These three sequences are presented in Figure 5 (*solid lines*) and correspond to three different total slab column densities N^{slab}_H. The intermediate sequence corresponds to the radiation-bounded case $N^{slab}_H = N_{H^*}$ (see § 2.3 for the operative definition of the depth of the photoexcited region N_{H^*}), a second sequence represents the matter-bounded case in which N^{slab}_H corresponds to the depth where hydrogen is 10% ionized (i.e., $N^{slab}_H \cong 2.4 \times 10^{20}\ \text{cm}^{-2}$), a third one is the case in which the NLR clouds are more massive than the radiation-bounded case and has $N^{slab}_H \equiv H_{H^*} + N^0_{H^0} = 5 \times 10^{21}\ \text{cm}^{-2}$, which is about 6 times the N_{H^*} of the dust-free case.[3] The zero-point

[3] Note that N_{H^*} progressively increases with μ, from $8 \times 10^{20}\ \text{cm}^{-2}$ when $\mu = 0$ to $2.6 \times 10^{21}\ \text{cm}^{-2}$ when $\mu = 1.25$. The main reason has to do with the criterion requiring that hydrogen be only 1% ionized at the inner boundary of the photoexcited region. Because the recombination coefficient depends on T_e, N_{H^*} becomes larger when the temperature of the PIZ increases as a result of depletion of the gas phase with increasing μ. We have found that T_e increases from 1200 K in the dust-free case to 3300 K at $\mu = 1.25$.

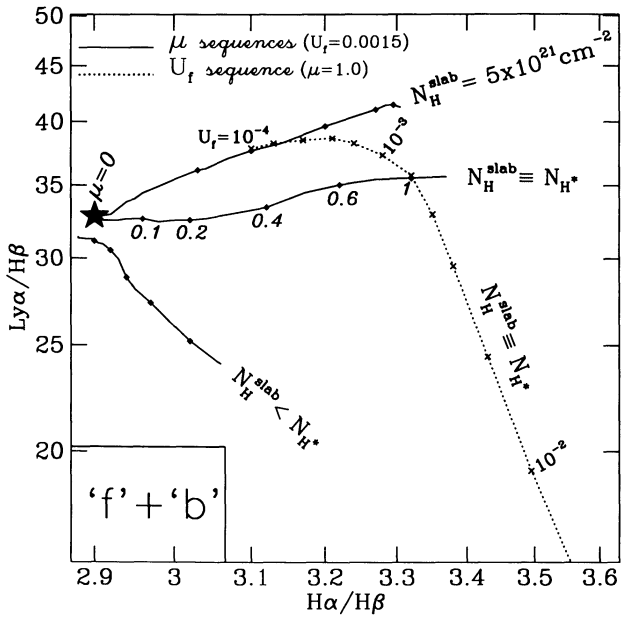

FIG. 5.—Lyα/Hβ as a function of the Balmer decrement for three sequences with $U_f = 0.0015$ in which μ is monotonically increasing ($0 \le \mu \le 1.25$). Tick marks from left to right along the solid lines indicate values of μ of 0.1, 0.2, 0.4, 0.6, and 1.0, respectively. The three sequences (*solid lines*) differ only by the total column density of the slab N^{slab}_H. The lowermost sequence is matter-bounded using the criterion that the hydrogen ionized fraction is 10% at the back layer. The intermediate sequence correspond to the radiation-bounded case without any additional neutral gas zone at the back. The uppermost sequence includes a neutral back zone such that the *total* column density of the slab is constant at $5 \times 10^{21}\ \text{cm}^{-2}$. The neutral and photoexcited zones are assumed to have the same dust content [$\mu(H^0) = \mu(H^*)$]. The filled star represents the reference dust-free case ($\mu = 0$). Also shown in the figure is an ionization parameter sequence (*dotted line*) for radiation-bounded slabs (with $N^0_{H^0} = 0$) of constant dust content $\mu = 1.0$ and covering the range $10^{-4} \le U_f \le 10^{-2}$. In all the above calculations, the ionizing energy distribution is a power law with index $\alpha = -1.4$, the gas density is $n^f_H = 5000\ \text{cm}^{-3}$ at the face of the cloud, the metals are depleted from the gas phase in accordance with the dust content μ, and the line intensities are given by the sum of the "f" and "b" perspectives.

dust-free reference model with $U_f = 0.0015$ model is represented in all figures by the filled star. We emphasize that our simple geometry assumes a very low volume filling factor of the emitting clouds so that as many "f" clouds as "b" clouds are seen by the observer without any intervening obscuration.

The most important result of the calculations shown in Figure 5 is to prove that despite large amounts of internal dust, the Lyα/Hβ calculated using canonical input parameters is not radically different from recombination case B, and, if anything, it can even be larger when $\mu \to 1$. The expected range for Lyα/Hβ in the dust-free recombination case B case is between 23 and 34 depending on the gas density. If, in addition, collisional excitation is present due to the hardness of the continuum or to low gas metallicity, both the Balmer and the Lyman decrement become larger (see Gaskell & Ferland 1984), a situation not unlike that shown in Figure 5 except that it is here the result of internal dust.

The two main factors explaining the relatively high Lyα/Hβ are that, first, with $U_f = 0.0015$, Lyα destruction is modest in the clouds since the column density of ionized gas and therefore $\tau_V(H^+)$ is not large, and second, the portion of the Balmer lines' flux which escape from the back is subject to considerable absorption by the dust inside the PIZ or within the neutral core of the cloud. It is therefore not surprising that the models

which depart most from case B Lyα/Hβ are those of the matter-bounded sequence. In this sequence, comparatively little absorption occurs for the Balmer lines while destruction of Lyα photons (which occur mostly in the fully ionized zone) remains significant (cf. § 3.2). To illustrate to what extent much higher values of U_f would be catastrophic to the escape of Lyα, the dotted line in Figure 5 represents an ionization parameter sequence with models of constant dust content ($\mu = 1.0$). Of course, these models are of limited relevance since they result in a forbidden-line spectrum incompatible with observed optical line ratios.

Since in the dust-free case we used solar metallicity for the gas, little collisional excitation takes place within the PIZ and the resultant Balmer decrement is not significantly above that of a dust-free H II region (Fig. 2*b*). With an ISM dust content of $\mu = 1$, however, the Balmer decrement in the radiation-bounded case is shown in Figure 5 to approach 3.3. On the other hand, moderate amounts of internal dust $\mu \approx 0.2$–0.4 would favor an intrinsic Balmer decrement in the range 3.0–3.1 assuming the clouds are radiation-bounded (the corresponding range for the Lyman decrement is 32–37). This range (3.0–3.1) corresponds to that proposed by various authors (Gaskell & Ferland 1984; Halpern & Steiner 1983) for the intrinsic NLR Balmer decrement except that it is here more the result of the presence of internal dust rather than of a hard ionizing continuum or of deficiencies in the gas metallicity relative to solar. Binette et al. (1990) pointed out the apparent lack of Seyfert 2 with Hα/Hβ < 3.4 if one considers only objects with good S/N in the Hγ line. If this high value of 3.4 was exclusively caused by internal dust present in all Seyfert 2's, then large values of μ (~ 1) are implied from Figure 5. Alternatively, a portion of the extinction may be the result of *intervening* gas containing dust, in which case the amount of *internal* dust implied is lower. There are two possibilities for how this intervening gas/dust may arise. In one case this dust is contained in a detached screen. Such models, however, may not be physically plausible as discussed in § 4.2. Another possibility is that the intervening dust + gas arises from a large covering factor of the NLR clouds themselves. This case is presented in § 4.3.

Radiation-bounded calculations with our selected parameters are known to over predict by a factor ≈ 2 the ratio [O I] λ6300/Hβ ratio. Using a moderately matter-bounded cloud such as the one shown in Figure 5, one can resolve this discrepancy by cutting the cloud at some depth to make the [O I] fit the observed value. As previously shown in Figure 4, the matter-bounded model with $\mu = 1$ results in a lower Lyα/Hβ (than radiation-bounded calculations) somewhat below case B and in a moderately reddened Balmer decrement. The procedure of cutting clouds to adjust [O I] to the observed value is, however, quite arbitrary. A more realistic approach is the dual gas components model of Viegas & Prieto (1992) which was proposed as a solution to explain the observed high He II/Hβ ratio observed in the spatially extended NLR (ENLR) (see also Morganti et al. 1991). This model consists of a matter-bounded (MB) and a radiation-bounded (RB) component. The MB component has a higher volume filling factor (to compensate for its much lower emission measure) and a higher ionization parameter ($U^{MB} > 0.0015$). Although we did not consider this level of complication in our modeling, we can still establish some of its general properties in relation to dust using the results of §§ 3.2 and 3.3. Under most instances, the effects of dust on the H I lines cannot be larger in the case of the dual-component model than with our simpler single RB component because the MB component, despite its higher U_f, is nevertheless extremely thin in column density and therefore generally results in little Lyα destruction.[4] Furthermore, the RB component should have $U^{RB} < 0.0015$ (Viegas & Prieto suggest $U^{RB} \leq 0.0006$) and therefore much lower τ_V than in our single RB component. In conclusion, a working dual-component model would in all likelihood be characterized by *smaller* line absorption effects due to dust at equal values of μ than in our simplified single component model.

4. DISCUSSION

After comparing calculations with internal dust with recent Lyα/Hβ data on Seyfert 2's (§ 4.1), we discuss various interpretations of the low values observed. We look at the possibility of pure line scattering or pure dust absorption (§ 4.2) as well as that of mutual covering of Lyα clouds (§ 4.3). On § 4.4, we consider the possibility of dust absorption of the UV continuum for explaining the apparent deficit of ionizing photons.

4.1. *Observational Data of KAW3*

The available data on the NLR Lyman decrement is still rather limited. The most reliable information on the NLR comes from Seyfert 2's since, as pointed out by FO86, only for these objects can one deduce an optical to ultraviolet line spectrum which is totally free of contamination by BLR components. It is likely, however, that the physical information gathered from the NLR of Seyfert 2 is relevant to that of Seyfert 1 and of quasars. One of the motivation of the current work was the recent publication by Kinney et al. (1991, hereafter KAW3) of a Seyfert 2 data set for which the optical spectra were taken through an aperture which matched the large *IUE* satellite aperture. The matching of aperture size for the different lines is a crucial point in the study of the NLR Lyman decrement because the emitting line region is spatially extended and in the likely event that Lyα, Hα, and Hβ present a different spatial distribution in surface brightness, the interpretation of ratios of lines derived from different apertures becomes very complicated, if not impossible. By comparing for instance objects common to both the KAW3 and FO86 data set, one finds many objects with significantly different line ratios between the two data sets presumably as a result of the much smaller aperture of the FO86 optical observations. For this reason we have limited our analysis to the data set of KAW3 which are presumed free of this problem.

In Figure 6 (which is an expanded scale version of Fig. 5), we present the data of KAW3 (*filled squares*) with their estimated error bars. The earlier model sequences of Figure 5 now appear as broken dash lines in the upper left. What is immediately striking is that internal dust absorption for an isotropic distribution of emitting clouds does not account for the low Lyα/Hβ ratios observed in *any* of the Seyfert 2's surveyed, nor the high Balmer decrement seen in at least a few of them. Interestingly, there are objects which present a near–case B Balmer decrement and yet a Lyα/Hβ ratio which is significantly below case B.

[4] The dual component model of Viegas & Prieto (1992) suggest a MB component with opacity $\tau^c_{H^0}(912\ \text{Å}) < 1$. Adopting $\tau^c_{H^0}(912\ \text{Å}) = 0.55$ and a similar $U^{MB} = 0.01$ to what they use, we obtain $N_H^{slab} \cong 1.4 \times 10^{20}\ \text{cm}^{-2}$ and $\tau_V \cong 0.067\mu$. Even with high dust content $\mu = 1$, our calculations indicate a Lyα destruction of only 0.13 dex with a difference in flux between "f" and "b" perspectives of 15%.

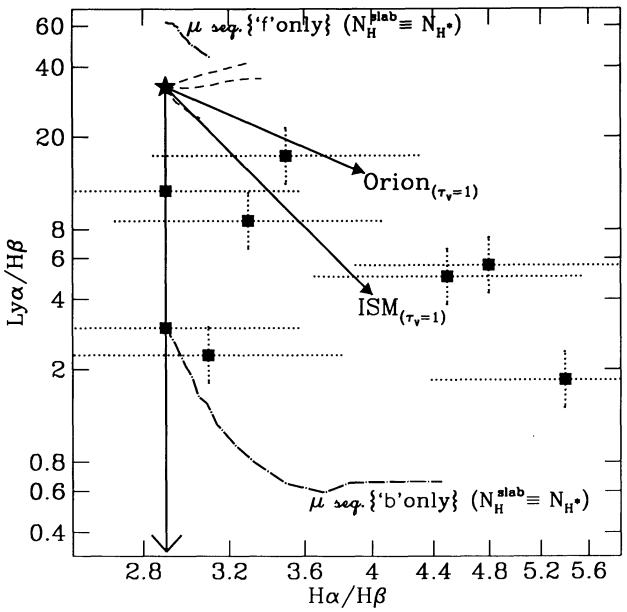

FIG. 6.—The squares represent the homogeneous data set of Seyfert 2 observations of Lyα/Hβ vs. Hα/Hβ by Kinney et al. (1991) in which the aperture in the optical closely matches the large-aperture *IUE* Lyα observations. Two reddening vectors corresponding to the ISM and the Orion extinction curve, respectively, are drawn to indicate the expected displacement due to foreground *pure* dust. The vectors' length correspond to an extinction $\tau_V = 1$ in the visible (5500 Å). The vertical solid line represents the effect of scattering of Lyα by a foreground neutral hydrogen screen at the same redshift as the NLR (see § 4.2). The dash-dotted lines represents the μ sequence with $U_f = 10^{-2.8}$ and $N^0_{H^0} = 0$ but as seen *separately* from perspective "f" and "b." The three dash lines correspond to the same μ sequences of Fig. 5 (i.e., with "f" + "b").

In order to explain the overall low Lyα/Hβ ratio in Seyfert 2's, either an intervening absorption/scattering screen is required or we must modify our simple NLR geometry. The first possibility, discussed in detail in § 4.2, would require pure line scattering from the screen to explain the near–case B Hα/Hβ objects, while a pure dust screen is required to explain the highly reddened Hα/Hβ objects. The second possibility is that the covering factor of the emission clouds is not small as was assumed so far. This idea is explored in § 4.3 along with the possibility that if the covering is extreme, a closed spherical geometry might be preferable to that of an isotropic distribution of slab-approximated clouds.

4.2. *The Pure Line Scattering and the Pure Dust Models*

There are broadly two types of Seyfert 2 objects in the KAW3 data: the objects with near–case B Hα/Hβ and the objects with reddened Hα/Hβ. The first category might be explained by pure Lyα scattering due to an intervening screen of H^0 which is supposed to be covering only the observer's view of the NLR but not the complete sky as seen from the NLR. Assume a slab geometry for the screen. Then for a pure scattering screen of thickness τ_{H^0scat}, where $\tau_{H^0scat} = 5.9 \times 10^{-14} N_{HI}^{screen} (T_{HI}/10^4\ K)^{-1/2}$ is the Lyα resonant scattering optical depth at line center, the fraction of photons impinging on the screen from the side facing the source which penetrates to the opposite side (the side facing the observer) is $\propto \tau_{H^0scat}^{-1/2}$ for $\tau_{H^0scat} \gg 1$ (Slater, Salpeter, & Wasserman 1982). Owing to the large magnitude of τ_{H^0scat}, only modest values of N_{HI}^{screen} are required to efficiently suppress the Lyα flux reaching the observer. Thus, for instance, for $N_{HI}^{screen} \sim 10^{15}$ cm^{-2} (10^{17} cm^{-2}), only ~10% (1%) of the incident Lyα photons reaches the observer; the rest are reflected back toward the source. At such column depths, the dust opacity within the screen is entirely negligible, and so the extinction vector shown in Figure 6 is purely vertical.

The lack of objects with near–case B Hα/Hβ in the FO86 sample has led these authors to propose pure dust absorption (ignoring the destruction of Lyα after multiple resonant scatters) since their objects all broadly lie along the ISM reddening vector (see Fig. 3 in FO86). Within the sample of KAW3, many objects still lie in the general direction of the ISM reddening vector. The pure dust screen (without any line scattering; otherwise, the reddening vector would be steeper than shown above) remains a possible interpretation for the observed ratios, but only for the reddened Hα/Hβ objects. Several limitations exist, however, with the picture of the pure dust screen which we now proceed to analyze.

In the pure dust screen model, a layer of dust and gas is presumed to lie outside the NLR toward the line of sight to the observer. Photons that pass through this layer are assumed to suffer solely absorption by the dust, that is, interaction between the photons and the gas are ignored. While this is a good approximation for non resonant line photons such as Hα and Hβ, it is a poor approximation for resonant line photons such as Lyα. Owing to the large resonant scattering cross section of Lyα photons, resonant scattering by these photons with neutral hydrogen atoms as they traverse the layer cannot be ignored in general. For example, to obtain a reddening of $A_V = 1$ requires $N_H = 2 \times 10^{21}$ cm^{-2} for $\mu = 1$. For a gas at $T_e = 10^4$ K, this corresponds roughly to $N_{HI} \sim 10^{20}$ cm^{-2}, which implies a line center resonant scattering optical depth for Lyα photons of $\tau_{H^0scat} \sim 6 \times 10^6$.

One possible way to avoid resonant scattering so that only pure dust absorption is operative is to have the layer move with a sufficiently large bulk velocity so that the line is shifted out of the Doppler core. How large a column density in neutral hydrogen can be tolerated without significant resonant scattering then depends on how fast the layer is moving away from the line source. We plot in Figure 7 this critical neutral hydrogen column density, N_{HI}^{crit}, against the layer bulk velocity for gas at $T_e = 10^2$, 10^4, and 10^6 K, where N_{HI}^{crit} is defined as the N_{HI} (measured in the comoving frame) that gives $\tau_{H^0scat} = 1$ (see Appendix B, § 1). Thus, resonant scattering may be ignored for layers with a neutral hydrogen column density lying below the curves. The "steps" in the curves corresponds to where the line is shifted from the core into the wings. It is evident that N_{HI}^{crit} is very low ($< 10^{14}$ cm^{-2}) unless the bulk velocity is very high. In order to have $A_V \gtrsim 1$, we require $N_{HI} \gtrsim 10^{20}$ cm^{-2}) (assuming $T_e = 10^4$ K and $\mu \approx 1$), which requires $V \gtrsim 500$ km s^{-1} from Figure 7. Aside from the issue of how to accelerate the layers to such high bulk velocities, there remains the problem that these clouds must be constantly replenished from some unknown source. This replenishing must be very efficient and continuous because the narrow-line ratios do not display significant variability. In addition, if the gas in the dust screen is at $T_e = 10^4$ K and has $N_{HI} \gtrsim 10^{20}$ cm^{-2}, the screen itself should have significant emissivity in lines such as Hα and Hβ, unless the screen is placed sufficiently far outside the NLR so that geometric dilution reduces the impinging ionizing flux to insignificant levels. Otherwise, one should see highly *blueshifted* lines (from the screen) in addition to the usual lines from the NLR. This is not observed.

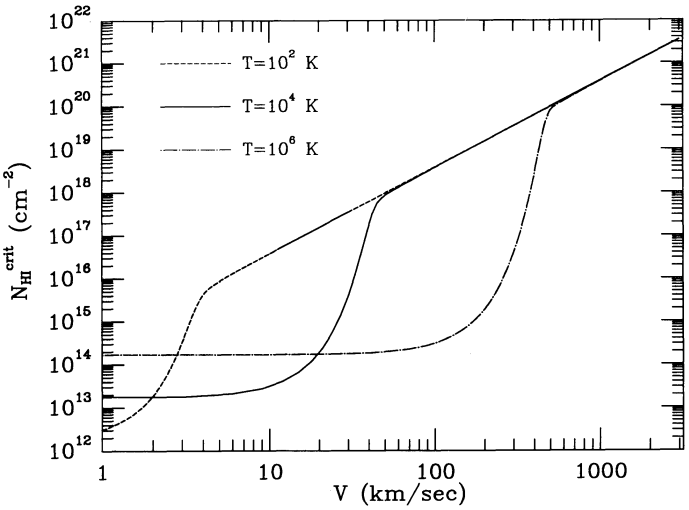

FIG. 7.—The critical neutral hydrogen column density, $N_{\rm HI}^{\rm crit}$, of the dust screen vs. the screen's bulk velocity, V. The quantity $N_{\rm HI}^{\rm crit}$ is defined as the column density (measured in the comoving frame) giving a Lyα resonant scattering optical depth of unity ($\tau_{\rm H^0scat} = 1$). The region below the curves have $\tau_{\rm H^0scat} < 1$. The curves correspond to a dust screen gas temperature of 10^2 K (*dashed*), 10^4 K (*solid*), and 10^6 K (*dot-dashed*). The "step" in each of these curves correspond to where the line is shifted from the core into the wings. The impinging Lyα line is assumed to be monochromatic at the line center (as measured in the line source frame).

Without invoking bulk motion, another way to make the pure dust screen viable is to make the gas in the dust screen very cold relative to the width of the line impinging on the screen. In this manner, only a very narrow band about line center will suffer resonant scattering within the screen. In Figure 8 we plot the fraction of the impinging energy in the Lyα line (assumed to have a Gaussian profile) that suffers interactions with neutral gas atoms in the screen as a function of the neutral hydrogen column density of the screen (see Appendix B, § 2). The horizontal line denotes where 1% of the incoming

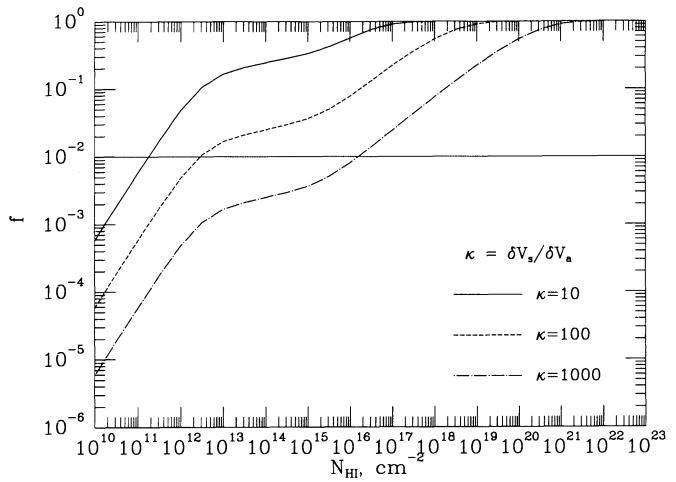

FIG. 8.—The fraction of energy, f, in the Lyα line impinging on the dust screen that suffers interactions with the screen's gas vs. the neutral hydrogen column density, $N_{\rm HI}$, of the screen. The horizontal dotted line correspond to $f = 0.01$. The curves correspond to $\kappa = \delta V_s/\delta V_a = 10$ (*solid*), 10^2 (*dashed*), and 10^3 (*dot-dashed*), where δV_s is the width (in velocity units) of the impinging Lyα line and δV_a is the width of the Lyα resonant scattering line profile for the gas in the dust screen.

line energy suffers interactions. The curves are labeled by the width of the impinging line (expressed in velocity units) relative to the width (in velocity units) across which the line will interact with the gas in the screen. Typical line widths for the NLR Lyα emission line is $\sim 10^3$ km s^{-1}. It is evident from Figure 8 that even for (screen) gas at $T_e = 10^2$ K so that $\kappa = \delta v_s/\delta v_a = 10^3$, the critical neutral hydrogen column density (to have 1% interaction or less) is only $\sim 10^{16}$ cm$^{-2} \sim N_{\rm H}$, corresponding to $A_V \sim 5 \times 10^{-6}\mu$. Thus, a cold screen is unfeasible because the low hydrogen column densities it requires (to avoid resonant scattering) imply negligible absorption by dust internal to the screen.

We conclude that either with bulk motion or with a very cold cloud, the pure dust screen model is not physically plausible. The only scenario we can conceive of where a pure dust screen might work is a "coronal" model wherein the dust is embedded in a *very* highly ionized, and hence very hot ($T_e \sim 10^6$ K), and tenuous ($n_e \sim 10$ cm^{-3}) medium. Assume for now that dust can exist in significant quantities in this coronal gas. To have $A_V \sim 1$ requires $N_{\rm H} \sim 10^{21}$ cm^{-2} for $\mu = 1$, or $N_{\rm H} \sim 10^{22}$ cm^{-2} for $\mu = 0.1$. With $n_e \sim 10$ cm^{-3}, this corresponds to a coronal region with linear size $L \sim 10^2$ pc ($\mu = 1$) or $L \sim 10^3$ pc ($\mu = 0.1$). In the former case, the size is comparable to the size of the NLR. While the existence of such a region external to the NLR cannot be ruled out, it is somewhat ad hoc. In the latter case, the large volume required for the coronal region almost surely implies that the corona would cover the whole NLR. In this case, one would expect the same dust in the coronal gas that affect the narrow lines to redden the starlight from the central galactic bulge. This reddening is generally not observed.

The properties of the coronal gas is probably not all that different from those of the intercloud medium in the NLR, if we assume a two-phase medium for the NLR with the two phases (cloud and intercloud) being in pressure equilibrium. If so, then postulating a separate corona outside the NLR seems superfluous; it would be more natural to assume dust to be present in the NLR intercloud medium itself. If, however, one is to consider dust in the intercloud medium, then one should also consider dust in the clouds themselves. The narrow lines produced within the NLR clouds would then be affected in general by dust in both the cloud and intercloud medium. With regard to dust survival, it is likely that both evaporation (owing to the high gas temperature) and sputtering will render the dust lifetimes to be shorter in the coronal-like intercloud medium than in the clouds. The main dust destruction process inside the clouds is sputtering which gives a dust lifetime of $\sim 10^5$ yr (assuming $n_e \sim 10^3$ cm^{-3} and $T_e \sim 10^4$ K). In the NLR model we adopt, we assume that dust is able to be replenished on such time scales inside the clouds to enable a significant dynamic steady state abundance of dust to be present. This replenishment is probably more difficult to achieve in the coronal-like intercloud medium, and in our model, we assume that dust is not present in any significant quantities in the intercloud medium.

4.3. *The Partially Covering Models*

One obvious advantage of a single interpretation for the position of all the objects in Figure 6 rather than the two separate pure dust and pure line scattering interpretations is that it might be more informative of the NLR geometry. Although the Lyα/Hβ observed is much below that predicted by the "f" + "b" models, some of the objects are not that far

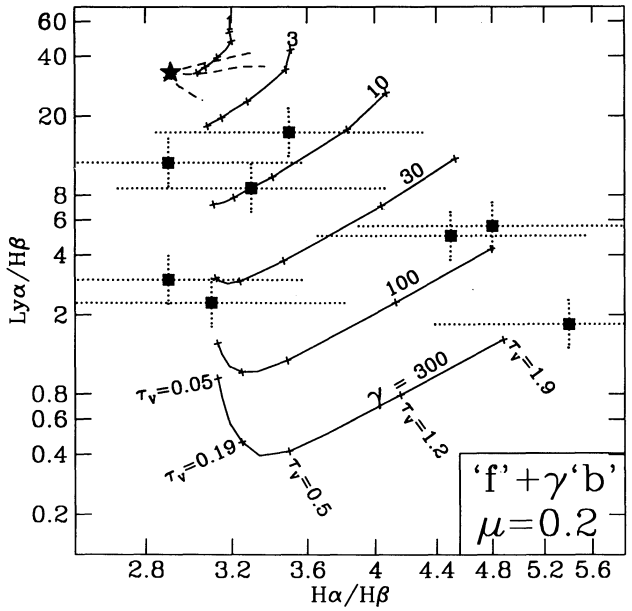

FIG. 9.—Same observations as in Fig. 6 but compared with the partially covering model using $\mu(H^*) = 0.2$ (see eq. [3]) and with the line fluxes obtained by giving a higher weight γ to perspective "b" ("f" + γ"b"). For a given value of γ, the solid line illustrates the effect of increasing the neutral zone depth, $N^0_{H^0}$, characterized by a dust content $\mu(H^0)$. The tick marks from left to right correspond to opacities of the $N^0_{H^0}$ zone of $\tau_V = 0.05$, 0.19, 0.5, 1.2, and 1.9 [for example, with $\mu(H^0) = 1.0$ these correspond to $N^0_{H^0} = 10^{20}$, 4×10^{20}, 10^{21}, 2.5×10^{21} and 4×10^{21} cm^{-2}, respectively]. The three dash lines correspond to the same μ sequences drawn in Fig. 5 ("f" + "b").

from the pure perspective "b" models (see dot-dash line in Fig. 6). This naively suggests a nonnegligible covering factor for the emission region in which individual clouds partly cover one another in the line of sight to the external observer. Although plane-parallel calculations do not allow us to replicate very accurately such a geometry, a first-order estimate of the effects involved can nevertheless be arrived at. For instance, we can safely expect the Lyα luminosity to be dominated by the few uncovered clouds which are directly seen from the front (i.e., "f" clouds). The Balmer lines in our simplified scheme would essentially come from three different components: the few "f" clouds seen directly, the many "b" clouds seen from the back, and finally the "f" clouds seen through other clouds and which we postulate are seen through a depth statistically equivalent to a single cloud (we neglect multiple cloud covering). By assuming that the transmitted spectrum of each covered "f" cloud is approximately equivalent to that of a "b" cloud,[5] we can readily estimate the main effects of a partially covered geometry by simply giving more weight to the "b" clouds, i.e., "f" + γ"b."

If Figure 9, we present the loci of "f" + γ"b" calculations in which the weight γ takes on the values of 1, 3, 10, 30, 100, and 300 using photoionization calculations in which the dust content $\mu(H^*) = 0.2$. For a given value of γ, the solid line tracks result from varying the depth of neutral gas $N^0_{H^0}$ (beyond the PIZ). Since the dust content within the neutral zone $\mu(H^0)$ (see eq. [3]) might plausibly be different from $\mu(H^*)$, we specify $N^0_{H^0}$ in Figure 9 in terms of the dust opacity in the visible, $\tau_V(H^0)$ [leaving $\mu(H^0)$ unspecified; see tick marks]. Considering the size of the error bars (*dotted lines*) which characterizes the data, we find very encouraging that the tracks pretty much cover the whole region occupied by all the Seyfert 2 observations.

Even if these tracks are only crude estimates and are not unique in terms of the parameter $\mu(H^*)$, they succeed in illustrating that a very simple and self-consistent mixture of internal line scattering and dust absorption can explain the observed ratios without the need for ad hoc intervening screens. We infer from this exercise that the NLR H I line ratios points toward a significantly self-covered distribution of gas which is very patchy and where all the Lyα originates from ionized gas in direct view of the observer.

If this conclusion is valid, it is possible to study one limiting case of this picture by supposing the covering factor to be so high that spherical geometry becomes a preferable representation of the NLR (and which at least addresses the effects of multiple scattering inside the geometry, a possibility excluded when considering only independent slabs).

Adopting spherical geometry, we will represent the NLR as a Strömgren sphere uniformly surrounded by a layer of neutral gas of opacity $\tau_V(H^0)$ except for a small area where the ionized sphere is not covered as depicted in Figure 10. As in the simple partial covering model discussed above, Lyα escapes exclusively from the region which is uncovered. The Balmer lines, on the other hand, emerge through both the uncovered area and the neutral dust outer layer.

To compute in spherical geometry and yet retain an adequate treatment of the transfer through dust, we integrate the emissivity of volume cells within either the near-side hemisphere "b" or the far-side hemisphere "f." For the line transfer we use the dust opacity occurring between each cell and the surface of the sphere along the direction of the observer's line of sight. The ionization and thermal structure as usual are calculated radially from the inner gas radius R_0 up to the limit of the photoexcited region R_*. For the line opacity, the integral extends out to include the outer neutral layer. The line emissivity cells are defined by the intersection of the photoionized spherical layers (used in the calculation of the radial ionization structure) of either hemisphere "f" or "b" with 10 concentric cylinders oriented along the lines of sight to the observer. In this scheme, we are in effect simulating the use of 10 concentric ring apertures of an observer which is looking at the spherical NLR. The global model is the sum of 10 "f" + "b" cylindrically integrated contributions.

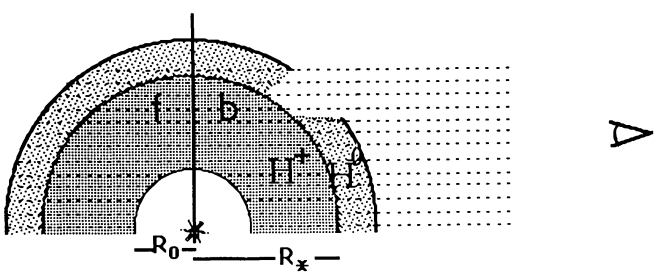

FIG. 10.—Schematic depiction of the spherical geometry assumed for the NLR. The photoexcited sphere of radius R_* and dust content $\mu(H^*)$ is divided into two hemispheres "f" and "b." The integral of the emissivity of each hemisphere is integrated along 10 concentric cylinders whose axis defines the observer's perspective. The photoexcited sphere is surrounded by a neutral shell of gas of dust content $\mu(H^0)$ and opacity $\tau_v(N^0_{H^0})$. A small area of the sphere is uncovered from which some Lyα can escape. The Lyα escape probability is determined radially starting from the inner gas radius R_0.

[5] A zeroth-order approximation based on the fact that the fully ionized zone is only a small fraction of the whole cloud and therefore any "b" spectrum is really seen through a screen of dust of depth comparable to that given by the whole slab.

Supposing no external neutral gas layer, we find that for the same amount of dust $\mu(H^*)$ and column density of ionized gas $N^S_{H^+}$, the spherical geometry results in a reduced Lyα/Hβ compared to the slab "f" + "b" case, resembling more in fact the "b" perspective of the slab case. This is understandable given that the direction of the gradient in ionization structure (n_{H^0}/n_H increasing with radius) seen by an observer external to the H^+ sphere is similar to that of a slab looked up from perspective "b." We emphasize that the effect of clumpiness of the ionized gas (which we do not consider in the transfer) would be more consistent with the geometry of a large number of clouds superposed along the line of sight. This would allow a larger fraction of Lyα to escape the ionized region as argued by Neufeld (1991), although the implementation of such effects is beyond the scope of this work.

To derive the emergent spectrum for the partially uncovered case, we simply combine the spectra of the fully covered sphere—excluding the contribution of a certain number of aperture rings—with the corresponding missing aperture rings of a spherical model calculated without any external gas layer covering the "b" hemisphere. Note that in the dust-free case, such procedure would underestimate the emerging Lyα by a factor of 2. With the presence of internal dust, the treatment is only approximate and rests on the reasonable assumption that most of the Lyα scattering is local to the point of emission, an approximation which is increasingly valid as μ is increased since a photon which would scatter too many times over a length scale of order R_* will likely be destroyed. Furthermore, the resonant photon does not know a priori where the hole in the outer layer is and will likely be absorbed in the much larger neutral outer zone which covers the ionized sphere.

The results are presented in Figure 11 where the amount of uncovered area is expressed as a fraction of the total projected emitting area πR_*^2. The parameters of the models were derived as follows. As for the slab case, we adjusted the ionization parameter of the spherical radiation-bounded models until [O III] λ5007/H$\beta \approx 10$ (by varying the source luminosity in the center and/or the volume filling factor of the infinitesimal gas filaments). The ionizing continuum is the same as before, the density at R_0 is 5000 cm^{-3} and the gas pressure is maintained constant with radius. The resulting photoexcited sphere in our calculations has $R_*/R_0 \approx 2.4$ and $N_{H^*} \approx 6.3 \times 10^{20}$ cm^{-2}. The electron column density is $N_e = 2.1 \times 10^{20}$ cm^{-2} which is exactly the same as for the reference slab model $\bar{U} = 0.0013$. Because more Lyα is destroyed in spherical geometry, we have assumed smaller values for $\mu(H^*)$, [See, for instance, the long dash line in Fig. 11 which correspond to models with $\mu(H^*) = 0.4$, a clearly excessive value.]

The solid lines in Figure 11 correspond to models with a small internal dust content $\mu(H^*) = 0.1$. The dust opacity of the external layer takes on the values of $\tau_V(H^0) = 0.5$ (*leftmost solid line*) and $\tau_V(H^0) = 2.4$ (*rightmost solid line*). From the position of the near–case B objects on the left, we infer that their NLR is probably less deeply embedded in dust [$\tau_V(H^0) \approx 0.5$] than the objects on the right [$\tau_V(H^0) \approx 2$–3]. The fraction of the uncovered area runs from 30% to as little as 3.0%–0.3%. Overall, the models bracket quite well the region occupied by the Seyfert 2 observations.

4.4. *Dust and the UV Continuum*

It is not clear how representative of Seyfert 2 the sample of KAW3 is since as many as five objects of the 12 objects in Figure 6 show evidence of properties assigned to Seyfert 1.

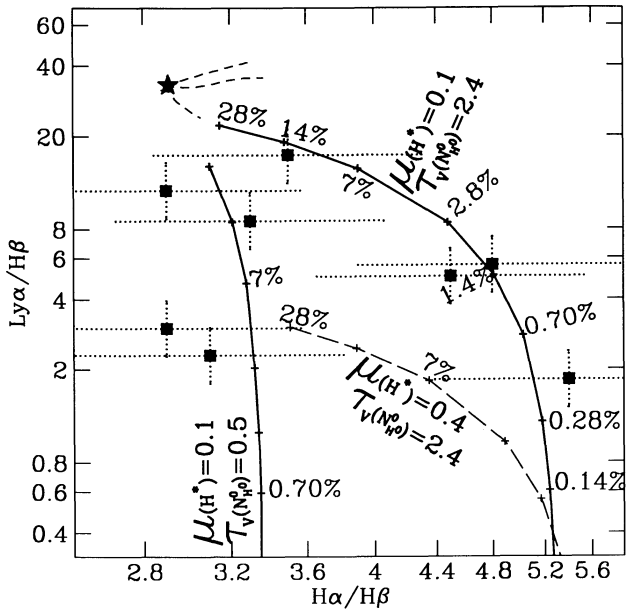

FIG. 11.—Same observations as in Fig. 6 but compared with the spherically closed geometry calculations. The ionized sphere is surrounded by an outer shell of neutral gas $N^0_{H^0}$ [with dust content $\mu(H^0)$; see eq. (3)] which we express in terms of dust opacity $\tau_V(H^0)$. The curves represent the effect of having a hole in this shell which directly expose part of the Strömgren sphere and allow some Lyα to escape out. Models with internal dust content $\mu(H^*) = 0.1$ and either $\tau_V(H^0) = 0.5$ or 2.5 are shown as solid lines. The long dash line corresponds to a model with a higher internal dust content in the ionized region with $\mu(H^*) = 0.4$. Tick marks along each curve represent the percentage of the uncovered area relative to the sphere's projected emitting area (πR_*^2).

These include either a very weak BLR either seen directly as in Mrk 348 and NGC 4388, or seen in polarized light as in Mrk 348, Mrk 3, and Mrk 463, or variability of the featureless continuum as in Mrk 477. Unification models of Seyferts have been proposed in which Seyfert 2's present a very thick torus which hides direct view of the BLR as a result of its inclination (see, for instance, Antonucci & Miller 1985; Krolik & Begelman 1988). Our conclusion from § 4.3 is that the ionized gas regions responsible for the emission lines are at least partly covered by large amounts of gas and dust with Lyα emerging from the least covered regions. According to this picture, we would expect the nuclear continuum to be reddened as well. We will present briefly some arguments which favor continuum reddening, a possibility earlier studied by Boisson & Durret (1986) (see also Carleton et al. 1987), although the idea of an extinction free continuum is more commonly accepted (e.g., FO86, KAW3).

KAW3 performed an important test on the photon budget of the nuclear engine by extrapolating the power laws which they had fitted to their *IUE* spectra and deriving the number of ionizing photons N^{obs}_{ion} which originates from the nucleus (assuming an isotropic source). After comparing with the number of recombination photons deduced from the Hβ luminosity N^{der}_{rec} (using the *dereddened* Hβ flux and assuming a covering factor of unity), they found that most objects showed a clear deficit of ionizing photons ($N^{der}_{rec}/N^{obs}_{ion} > 1$), which they concluded as favoring the "occulation/ reflection picture" of Antonucci & Miller (1985). According to this picture, the ionizing photons stream out freely only along the axis of the torus axis and are sufficiently numerous to account for the luminosity of the H I recombination lines (although the continuum

observed in our direction [off-axis] is too weak to account for them).

Although the "occultation/reflection picture" is supported by other independent arguments, there remains, however, an unresolved paradox (see Binette, Fosbury, & Parker 1993): if Hβ of the large NLR is so much reddened (and considering a closed geometry for the NLR), why is the nuclear continuum of comparatively pointlike size not reddened at all? Interestingly, using other *IUE* Seyfert observations, Boisson & Durret (1986) as well as Carleton et al. (1987) concluded that there is no deficit of ionizing photons if dereddening of the nuclear continuum is taken into account. The important argument against continuum reddening given by KAW3 is that the 2175 Å ($10^{15.14}$ Hz) dust absorption feature was not present in their featureless continua. Although this seems to be clearly the case for objects like NGC 1068, we are not strongly convinced that this feature is totally absent from some of their spectra given the noise level present. In particular, objects like Mrk 3 and possibly NGC 4388 show plausible hints of such a feature. Furthermore, the absence of the 2175 Å feature is not so compelling if we consider the possibility that the properties of the dust in AGNs might differ from that in the Galaxy. After all, we know that dust grain properties depend strongly upon the environment in which they form (Whittet 1992).

One way of addressing the issue of extinction of the nuclear "nonstellar" continuum is too look at possible hints of correlation of the inferred deficit of ionizing photons with the *IUE* spectral index as well as with the amount of reddening inferred from the Balmer decrement. We present in Figure 12 the results of such an attempt based upon the KAW3 data set. Note that we plotted in abscissa the quotient $N_{\rm rec}^{\rm obs}/N_{\rm ion}^{\rm obs}$ which differ from KAW3 in that it is based on the observed Hβ *not* corrected for reddening (since we want to model all the observed quantities as a function of extinction). Although the correlations of Figures 12*a* and 12*b* are not statistically significant, given the magnitude of the errors, the data is not inconsistent with a simple reddening model (*solid line*) described below and applied to an intrinsic power law of index $\alpha = -0.3$ (assuming the gas covering factor and the continuum's shape to be intrinsically the same in *all* the objects).

To obtain the theoretical results represented by the solid line in Figure 12, we illuminate isotropically a slab of dust with opacity τ_V with an $\alpha = -0.3$ power-law continuum and compute the transmitted spectrum from this slab. We calculate a one-parameter sequence of slab models in τ_V. For each model, we compute the emergent reddened α (defined by the flux ratios at 2450 Å and 1310 Å in the calculated transmitted spectrum). We present in Figure 12*a* the effect of increasing dust extinction (τ_V) on the observed $N_{\rm rec}^{\rm obs}/N_{\rm ion}^{\rm obs}$ starting with an unreddened value $(N_{\rm rec}/N_{\rm ion})_0 = 0.15$, corresponding to a gas covering factor of 15% (varying the covering factor simply slides the curve horizontally). In Figure 12*b* we present the results of increasing τ_V on the Balmer decrement assuming an intrinsic ratio of 3.1. The standard extinction curve has been assumed in our model. Details on the transfer solution for the continuum and for the lines are given in Appendix C.

We have assumed the impinging flux to be isotropic in order to approximate a shell layer of dust illuminated by a pointlike central source; a more appropriate treatment which distinguishes the isotropic optical lines from the radio continuum flux will be the subject of subsequent work. Because both the continuum and Hβ are reddened by the same amount of dust, the equivalent width of Hβ is independent of τ_V in our slab treatment. Although the index $\alpha = -0.3$ is rather flat, it is not

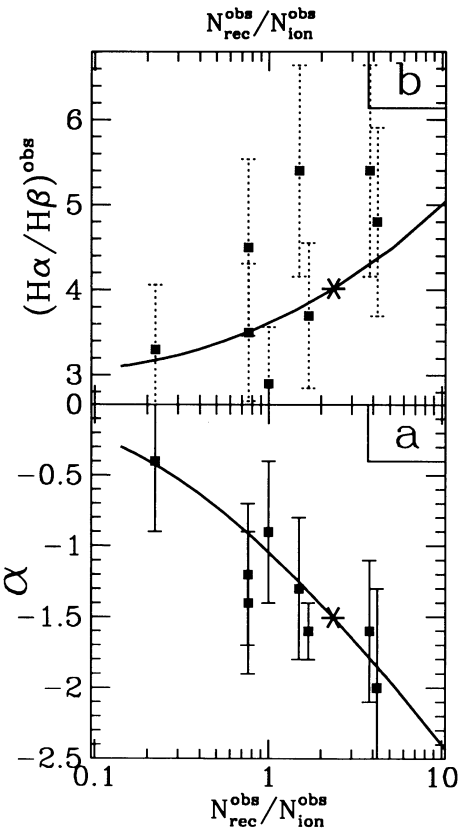

FIG. 12.—In panel (*a*), the power-law index α vs. the ratio $N_{\rm rec}^{\rm obs}/N_{\rm ion}^{\rm obs}$. The spectral index α corresponds to the power-law fit by KAW3 of the observed continuum energy distribution between 2600 Å and 1300 Å. In panel (*b*), the observed Balmer decrement is plotted as a function of $N_{\rm rec}^{\rm obs}/N_{\rm ion}^{\rm obs}$. The ratio $N_{\rm rec}^{\rm obs}/N_{\rm ion}^{\rm obs}$ differs from KAW3 in that the *observed* value of the Hβ flux is used to derive the number of recombination photons instead of using the reddening-corrected Hβ flux. The solid line is a model representing the effect of increasing dust extinction on an intrinsic power-law ionizing continuum of index $\alpha = -0.3$ assuming a covering factor of 15% (panel [*a*]) and an intrinsic Balmer decrement of 3.1 (panel [*b*]). The apparent index α of the calculated transmitted spectrum is derived by simply using the flux ratios at 2450 Å and 1310 Å. The star represents the locus of a model with a shell dust extinction of $\tau_V = 1.3$.

at odds with the range −0.08 to +0.11 denoted by Shuder (1981) (for the case of a covering factor of 10%) in his study of the proportionality between continuum and Hα luminosities in various classes of AGNs (see also Binette, Fosbury, & Parker 1993).

Comparing Figures 12*a* and 12*b*, the slope of the model in the case of the Balmer decrement panel seems too low. This could be a consequence of an inhomogeneous covering of the nuclear dust as proposed in § 4.3 for the H I lines (Figs. 10 and 11). Since $N_{\rm rec}^{\rm obs}/N_{\rm ion}^{\rm obs}$ and α depend mostly on the UV part of the spectrum which is very sensitive to small amounts of dust, these quantities are expected to be strongly weighted toward the least obscured regions, while the optical Balmer lines may emerge from more obscured regions.

Despite the recognized validity of the "occultation/reflection picture" in explaining cones of ionization and hidden polarized BLR in some Seyfert 2's, it remains important to test further whether the nuclear continuum is as reddening free as generally assumed and, therefore, whether part of the apparent deficit in the ionizing radiation does not simply result from dust extinction.

APPENDIX A

The term depletion refers to the underabundance of gas phase elements with respect to the solar standard abundances as a result of their assumed presence in dust. References to the studies of depletion in the local ISM can be found in Whittet (1992). We describe here a *theoretical* algorithm which attempts to deplete in a meaningful way the trace element abundances when computing line diagnostics for a plasma of arbitrary *gas* metallicity $Z_{\rm gas}$ and dust content μ. Both quantities $Z_{\rm gas}$ and μ ($\propto Z_{\rm dust}$; see eq. [A5]) are known to depart significantly from solar neighborhood values in low-mass extragalactic systems or as a function of galactic radius in the Galaxy. For the purpose of modeling plasma conditions in a nonsolar environment, we defined an algorithm which scales in a self-consistent manner the depletion of the gas phase in proportion to the quotient μ/Z, where Z is the *total* metallicity of the plasma ($Z = Z_{\rm dust} + Z_{\rm gas}$) expressed *relative* to local ISM values:

$$Z = \frac{\sum m_{\rm X}(\{n_{\rm X}\}_{\rm dust} + \{n_{\rm X}\}_{\rm gas})_{\rm plasma}}{\sum m_{\rm X}\{n_{\rm X}\}_{\odot}}\,, \tag{A1}$$

and μ is the dust content of the plasma expressed *relative* to that of the standard ISM dust-to-gas mass ratio. The reference solar abundances set which we adopt is taken from the compilation of Anders & Grevesse (1989) and is listed in Table A1 (see entry $\{n_{\rm X}/n_{\rm H}\}_{\odot}$). We define D(X), the depletion index of element X, as

$$D(\mathrm{X}) = \left[\frac{\mathrm{X}}{\mathrm{H}}\right] = \log\left\{\frac{n_{\rm X}\,L}{n_{\rm H}\,L}\right\}_{\rm ISM} - \log\left\{\frac{n_{\rm X}}{n_{\rm H}}\right\}_{\odot}\,, \tag{A2}$$

where $\{n_{\rm X}\,L/n_{\rm H}\,L\}_{\rm ISM}$ represents the ratio of the column densities of the gaseous element X (measured along various lines of sight of path length $L[\lesssim 6 \times 10^{20}$ cm]) over the corresponding measured column densities of H. In the local ISM, the number density of atoms $n_{\rm X}$ of element X which are found either in gas form (or depleted into dust grains) is given relative to $n_{\rm H}$ by $\{n_{\rm X}/n_{\rm H}\}_{\odot}\ 10^{D(\mathrm{X})}[$or $\{n_{\rm X}/n_{\rm H}\}_{\odot}\ [1 - 10^{D(\mathrm{X})}]]$. The adopted set of local ISM depletion indices D(X) is listed in Table A1 and was derived from Table 2.2 of Whittet (1992) except for carbon for which the value -0.5 was adopted as suggested by some authors. This value is also consistent with our dust model which includes graphite grains.

For the local ISM, for which $\mu \equiv 1$ (and $Z = Z_{\rm dust} + Z_{\rm gas} = 1$), the gas phase abundances are derived directly from the depletion indices of Table A1. As we are often interested in modeling line emission plasma with $Z \neq 1$, we could assume that the dust content μ scales linearly with Z. That this is approximately true is supported by the results of Issa, MacLaren, & Wolfendale (1990) and Sauvage & Vigroux (1991) who compared the metallicity and extinction in the Galaxy with those of the Magellanic Clouds or of nearby spirals. In our calculations, if we adjusted the dust content such that always $\mu/Z = 1$, assuming that the depletion indices of Table A1 remain approximately valid, the procedure for depletion is straightforward and the gas phase abundance by number of element X is simply given by

$$\{n_{\rm X}/n_{\rm H}\}_{\rm gas} = Z\{n_{\rm X}/n_{\rm H}\}_{\odot}\ 10^{D(\mathrm{X})}\,. \tag{A3}$$

This is equivalent in saying that when $\mu/Z = 1$ both the dust grains as well as the gas phase are made up of the same *relative* proportion of trace elements.

For the more general case where $\mu \neq Z$, we have no observational basis as to how the depletion indices might vary. If we use the local ISM indices as a guess of the depleted abundances and then simply renormalize the whole abundance set by a constant factor until the depleted mass match the value implied by μ (see eq. [A5] below), we obtain in the case $\mu \ll Z$ rather implausible gas abundances for some of the elements. To alleviate this problem, we have chosen instead to vary the depletion indices in some proportion to the ratio μ/Z before linearly renormalizing the total mass of the depleted metals. An indication of the relative variation of the depletion indices D(X) with the ratio μ/Z can be intuitively inferred from the measured quantities $\{r_n/r_N\}_{\rm X}^{\rm ISM}$ which represents the ratio for element X of the correlation coefficient of D(X) with density, r_n, over the correlation coefficient of D(X) with column density, r_N. The merits of the measured $\{r_n/r_N\}_{\rm X}^{\rm ISM}$ ratios is that they sample regions of somewhat different dust content μ. The algorithm we devised for each case $\mu \neq Z$ is the following: we first define modified depletion indices $D(\mathrm{X}, \mu/Z)'$ which are

TABLE A1

SOLAR ABUNDANCES BY NUMBER, ISM DEPLETION INDICES, AND CORRELATION COEFFICIENT RATIOS

Element	$\{n_{\rm X}/n_{\rm H}\}_{\odot}$	$D(\mathrm{X})_{\rm ISM}$	$\{r_n/r_N\}_{\rm X}^{\rm ISM}$
H	1.000	...	...
He	0.1	0.0	...
C	3.6×10^{-4}	−0.5	0.88
N	1.1×10^{-4}	−0.1	0.46
O	8.5×10^{-4}	−0.2	0.42
Ne	1.2×10^{-4}	−0.0	...
Mg	3.8×10^{-5}	−0.7	1.11
Si	3.5×10^{-5}	−1.6	1.19
S	1.9×10^{-5}	−0.2	0.94
Ar	3.6×10^{-6}	0.0	...
Ca	2.2×10^{-6}	−3.7	1.42

dependent on μ/Z as follows

$$D(\mathrm{X}, \mu/Z)' = D(\mathrm{X})\left(\frac{\mu}{Z}\right)^{\gamma\{r_n/r_N\}\mathrm{X}} . \tag{A4}$$

By trial and error, we established that $\gamma = 0.25$ gave a reasonable behavior of the depleted elements even when $\mu/Z \rightarrow 0$. The values we adopted for $\{r_n/r_N\}_{\mathrm{X}}^{\mathrm{ISM}}$ (see Table A1) were derived from Figure 2.9 of Whittet (1992). Linear renormalization of the abundances implied by the modified indices $D(\mathrm{X}, \mu/Z)'$ is required in order that the mass of the elements depleted unto dust grain remains consistent with the value of μ. This is done in an iterative fashion by determining the value of δ (≈ 1) until the following dust mass equation is satisfied

$$Z_{\mathrm{dust}} \sum m_{\mathrm{X}}\{n_{\mathrm{X}}\}_{\odot} = 0.0089\mu \frac{m_{\mathrm{H}}\{n_{\mathrm{H}}\}}{\sum m_{\mathrm{X}}\{n_{\mathrm{X}}\}} = Z \sum \left\{\frac{m_{\mathrm{X}} n_{\mathrm{X}}}{m_{\mathrm{H}} n_{\mathrm{H}}}\right\}_{\odot} [\![1 - \kappa \min [1, \delta 10^{D(\mathrm{X}, \mu/Z)'}]]\!] , \tag{A5}$$

where the constant 0.0089 represents the dust-to-gas mass ratio relative to H (i.e., $\rho_{\mathrm{dust}}/\rho_{\mathrm{H}}$) of any of the extinction curves computed by P. G. Martin (this number is consistent with the ISM value if our dust composition within the grain model is valid). The constant $\kappa = 1.123$ is a small correcting factor to allow for the fact that the summation is limited to the elements of Table A1 (considered by MAPPINGS) which does not include all the depleted elements (e.g., Fe). Once δ is determined, the gas phase abundance of any element X is

$$\{n_{\mathrm{X}}/n_{\mathrm{H}}\}_{Z,\mu}^{\mathrm{gas}} = Z\{n_{\mathrm{X}}/n_{\mathrm{H}}\}_{\odot} \min [1, \delta 10^{D(\mathrm{X}, \mu/Z)'}] . \tag{A6}$$

The value of κ is such that δ becomes unity if $\mu/Z = 1$ in which case equation (A5) reduces to equation (A3). With the above depletion algorithm, as $\mu/Z \rightarrow 0$, the uncertainty on the absolute abundances of the highly depleted elements (e.g., Ca) is probably quite high but since no observational depletion data for $\mu/Z \ll 1$ is available, this situation cannot be helped. The main purpose of our algorithm was that it gave a cumulative depletion of the gas phase elements always consistent with the dust content μ. Furthermore, as $\mu/Z \rightarrow 0$ it also has the property of giving for *all* the elements concerned much more plausible values than any alternative linear scheme which we could devise. The need of a depletion algorithm even if imperfect is called for in any photoionization calculation which purport to explore the regime $\mu < 1$ and $Z = 1$. This is, moreover, a likely regime for the warm emission-line ionized gas since it is quite conceivable that the dust content is lower than the ISM as a result of destruction of dust grains by sputtering (although the timescales are relatively long compared to the lifetime of an H II region; see Osterbrock 1989) or as a result of segregative acceleration away from the cloud of much of the smaller grains' population due to radiation pressure.

APPENDIX B

1. CALCULATION OF $N_{\mathrm{H\,I}}^{\mathrm{crit}}$

We assume a slab geometry for the screen. For an isothermal screen with H I column density $N_{\mathrm{H\,I}}^{\mathrm{screen}}$, the optical depth for Lyα resonant scattering is

$$\tau(x) = N_{\mathrm{H\,I}}^{\mathrm{screen}} \sigma_0(T)\phi(x) , \tag{B1}$$

where $x = (\omega - \omega_0)\omega_{\mathrm{D}}$, $\sigma_0(T)\phi(x)$ is the thermally averaged resonant scattering cross section,

$$\sigma_0(T) = 5.9 \times 10^{-14}(T/10^4\ \mathrm{K})^{-1/2}\ \mathrm{cm}^2 , \tag{B2}$$

$$\phi(x) = \frac{a}{\pi} \int_{-\infty}^{+\infty} \frac{e^{-y^2}\, dy}{a^2 + (x - y)^2} , \tag{B3}$$

$a = \Gamma/2\omega_D = 4.7 \times 10^{-4}(T/10^4\ \mathrm{K})^{-1/2}$ is the damping constant with Γ^{-1} the radiative lifetime of the excited state, and $\omega_{\mathrm{D}} = \omega_0(2k_B T/m_{\mathrm{H}} c^2)^{1/2}$ is the thermal Doppler width with $\omega_0/2\pi = 2.47 \times 10^{15}$ Hz the line center (Lyα) frequency (Bonilha et al. 1979).

For photons of frequency ω_i and direction cosine $\boldsymbol{n}_i$ injected into a screen moving at velocity $\boldsymbol{v}$, we evaluate the optical depth (a Lorentz scalar) in the cloud (comoving) frame to obtain

$$\tau(\omega_{\mathrm{cloud}}) = N_{\mathrm{H\,I}}^{\mathrm{screen}} \sigma_0(T)\phi(\omega_{\mathrm{cloud}}, T) , \tag{B4}$$

where $\omega_{\mathrm{cloud}} = \gamma\omega_i(1 - \boldsymbol{v} \cdot \boldsymbol{n})$ and $\gamma = (1 - v^2)^{-1/2}$. For line center injection, $\omega_i = \omega_0$, and the column density at which $\tau(\omega_{\mathrm{cloud}}) = 1$, $N_{\mathrm{H\,I}}^{\mathrm{crit}}$, is then given by

$$N_{\mathrm{H\,I}}^{\mathrm{crit}} = \frac{1}{\sigma_0(T)\phi(\omega_{\mathrm{cloud}}, T)} = N_{\mathrm{H\,I}}^{\mathrm{crit}}(v) . \tag{B5}$$

2. CALCULATION OF f

Let $N(x)$ be the flux of Lyα photons impinging on a screen which we model as a plane parallel slab. The width of the impinging line feature is δV_s (in km s^{-1}) so that $x = (\omega - \omega_0)/(\omega_0\, \delta V_s)$. Let the width of the Lyα resonant scattering line profile in the screen be given by δV_a (in km s^{-1}). The probability that a line photon will suffer an interaction when traversing the screen is $1 - e^{-\tau(x')}$, where $\tau(x')$ is given by equation (B1), and $x' = (\omega - \omega_0)/(\omega_0\, \delta V_a) = \kappa x$ with $\kappa \equiv V_s/\delta V_a$. The fraction of Ly$\alpha$ photons that suffers inter-

actions when traversing the screen is then

$$f = \frac{\int_{-\infty}^{+\infty} dx\, N(x)[1 - e^{-\tau(x')}]}{\int_{-\infty}^{+\infty} dx N(x)} = f(N_{\rm H\,I}^{\rm screen};\, \kappa)\,. \tag{B6}$$

Taking $N(x) \propto e^{-x^2}$ gives

$$f = \pi^{-1/2} \int_{-\infty}^{+\infty} dx\, e^{-x^2}[1 - e^{-\tau(x')}]\,. \tag{B7}$$

Equation (B6) also gives the fraction of the impinging Lyα energy flux that interacts with the H I gas in the screen since the impinging energy flux of Lyα is approximately $\hbar\omega_0 N(x)$.

APPENDIX C

The transfer of the UV continuum across an arbitrary thick slab of dust which is discussed in § 4.4 was carried out using the numerical solution described in detail by Magris (1985; see also Bruzual et al. 1988). Let us consider an arbitrary frequency with its corresponding absorption ($\sigma_{\rm abs}$) and scattering ($\sigma_{\rm sca}$) dust cross sections. We are interested in solving the following transfer equation

$$\mu \frac{dI(\tau,\, \mu)}{dt} = I(\tau,\, \mu) - S^S(\tau,\, \mu)\,, \tag{C1}$$

where $d\tau = -(\sigma_{\rm sca} + \sigma_{\rm abs})dx$ is the differential optical depth of the medium. This equation which takes into account scattering as well as absorption by homogeneously distributed dust particles is appropriate to the plane parallel geometry case. The scattering source function due to the dust grains is given by

$$S^S = \frac{a}{4\pi} \int I(\tau,\, \mu)\Phi(\theta) d\Omega\,, \tag{C2}$$

where $a = \sigma_{\rm sca}/(\sigma_{\rm sca} + \sigma_{\rm abs})$ is the albedo and $\Phi(\theta) = (1 - g^2)/(1 + g^2 - 2g\cos\theta)^{3/2}$ is the scattering phase function. The phase function is characterized by the asymmetry parameter $g = \langle\cos\theta\rangle$ with θ the scattering angle and g the Henyey-Greenstein asymmetry parameter characterizing our dust grain models and tabulated by P. G. Martin as a function of frequency along with $\sigma_{\rm abs}$ and $\sigma_{\rm sca}$ (see grain model in Martin & Rouleau 1991). The transfer equation was solved by using the finite difference solution method of Milkey, Shine, & Mihalas (1975) with the following boundary conditions:

$$\begin{aligned} I(\tau,\, \mu) &= 0 \qquad \text{for} \qquad \tau = 0, \quad \mu < 0 \\ I(\tau,\, \mu) &= I_c \qquad \text{for} \qquad \tau = T_{\rm ext},\ \mu > 0\,, \end{aligned} \tag{C3}$$

where $T_{\rm ext}$ is the optical depth of the slab and I_c is the intensity of the incident continuum radiation which illuminates *isotropically* one side of the dust slab. To obtain the numerical solution, we use a logarithmically uniform mesh that is symmetric about slab center. The integrations over angle were carried out by using the Gauss quadrature method (e.g., Chandrasekhar 1960) with five points. In order to test the accuracy of our numerical solution, we have compared our results with the analytical solution of Roberge (1983). In particular, we could reproduce very well the behavior of the mean intensity versus optical depth inside the slab when illuminated isotropically on both surfaces.

REFERENCES

Anders, E., & Grevesse, N. 1989, Geochim. Cosmochim. Acta, 53, 197
Antonucci, R. R., & Miller, J. S. 1985, ApJ, 297, 621
Baldwin, J. A., Ferland, G. J., Martin, P. G., Corbin, M. R., Cota, S. A., Peterson, B. M., & Slettebak, A. 1991, ApJ, 374, 580
Barvainis, R. 1992, ApJ, 400, 502
Binette, L., Calvet, N., Cantó, J., & Raga, A. C. 1990, PASP, 102, 723
Binette, L., Dopita, M. A., & Tuohy, I. R. 1985, ApJ, 297, 476
Binette, L., Magris C., M., Fosbury, R. A. E., Martin, P. G., & di Serego Alighieri, S. 1993a, in preparation
Binette, L., Fosbury, R. A. E., & Parker, D. 1993, PASP, submitted
Binette, L., Wang, J. C. L., Zuo, L., & Magris C., M. 1993b, AJ, 105, 797 (BWZM)
Boisson, C., & Durret, F. 1986, A&A, 168, 32
Bonilha, J. R. M., Ferch, R., Salpeter, E. E., Slater, G., & Noerdlinger, P. D. 1979, ApJ, 233, 649
Bruzual A., G., Magris C., G., & Calvet, N. 1988, ApJ, 333, 673
Carleton, N. P., Elvis, M., Fabbiano, G., Willner, S. P., Lawrence, A., & Ward, M. 1987, ApJ, 318, 595
Chandrasekhar, S. 1960, Radiative Transfer (New York: Dover)
Cimatti, A., di Serego Alighieri, S., Fosbury, R. A. E., Salvati, M., & Taylor, D. 1993, MNRAS, in press
Clavel, J., Wamsteker, W., & Glass, I. S. 1989, ApJ, 337, 236
Cohen, R. D. 1983, ApJ, 273, 489
Crosas, M. 1993, Ap&SS, in press
De Zotti, G., & Gaskell, C. M. 1985, A&A, 147, 1
DeRobertis, M. M., & Osterbrock, D. E. 1984, ApJ, 286, 171
DeRobertis, M. M., & Osterbrock, D. E. 1986, ApJ, 301, 727
Draine, B. T. 1978, ApJS, 36, 595
Ferland, G. J., & Netzer, H. 1979, ApJ, 229, 274
———. 1983, ApJ, 264, 105
Ferland, G. J., & Osterbrock, D. E. 1985, ApJ, 289, 105
———. 1986, ApJ, 300, 658 (FO86)
Filippenko, A. V. 1985, ApJ, 289, 475
Fosbury, R. A. E. 1993, in The Nature of Compact Objects in AGN, ed. A. Robinson & R. J. Terlevich (Cambridge: Cambridge Univ. Press), in press
Gaskell, C. M. 1984, Ap. Letters, 24, 43
Gaskell, C. M., & Ferland, G. J. 1984, PASP, 96, 393
Halpern, J. P., & Steiner, J. E. 1983, ApJ, 269, L37
Hummer, D. G., & Kunasz, P. B. 1980, ApJ, 236, 609
Hummer, D. G., & Storey, P. J. 1987, MNRAS, 224, 801
Issa, M. R., MacLaren, I., & Wolfendale, A. W. 1990, A&A, 236, 237
Johnson, L. C. 1972, ApJ, 174, 227
Kinney, A. L., Antonucci, R. R. J., Ward, M. J., Wilson, A. S., & Whittle, M. 1991, ApJ, 377, 100 (KAW3)
Krolik, J. H., & Begelman, M. C. 1988, ApJ, 329, 702
Kwan, J., & Krolik, J. H. 1981, ApJ, 250, 478
Magris C., G. 1985, in senior physics thesis, Universidad Simón Bolívar and CIDA, Venezuela
Magris C., G., Binette, L., & Martin, P. G. 1993, Ap&SS, in press
Malkan, M. A. 1983, ApJ, 264, L1
Martin, P. G., & Rouleau, F. 1991, in Extreme Ultraviolet Astronomy, ed. R. F. Malina & S. Bowyer (Oxford: Pergamon), 341

Milkey, R. W., Shine, R. A., & Mihalas, D. 1975, ApJ, 202, 250
Morganti, R., Robinson, A., Fosbury, R. A. E., di Serego Alighieri, S., Tadhunter, C. N., & Malin, D. F. 1991, MNRAS, 249, 91
Netzer, H. 1993, in The Nearest Active Galaxies, ed. L. Colina, J. Bachman, & A. Diaz, in press
Netzer, H., & Laor, A. 1993, ApJ, 404, L51
Neufeld, D. A. 1990, ApJ, 350, 216.
———. 1991, ApJ, 370, L85
Osterbrock, D. E. 1989, Astrophysics of Gaseous Nebulae and Active Galactic Nuclei (Mill Valley: University Science Books)
Pelat, D., Alloin, D., & Fosbury, R. A. E. 1981, MNRAS, 195, 787
Pier, E. A., & Krolik, J. H. 1992, ApJ, 401, 99
Puetter, R. C., & Hubbard, E. N. 1987, ApJ, 320, 85
Roberge, W. G. 1983, ApJ, 275, 292
Sanders, D. B., et al. 1989, ApJ, 347, 29
Sauvage, M., & Vigroux, L. 1991, in IAU Symp. 148, The Magellanic Clouds, ed. R. Haynes & D. Milne (Dordrecht: Kluwer), 407
Shuder, J. M. 1981, ApJ, 244, 12
Shull, J. M., & Van Steenberg, M. 1985, ApJ, 298, 268
Slater, G., Salpeter, E. E., & Wasserman, I. 1982, ApJ, 255, 293
Tadhunter, C. N., Robinson, A. & Morganti, R. 1989, in Extragalactic Activity in Galaxies, ed. R. A. E. Fosbury & E. A. J. Meurs (Garching: ESO), 293
Viegas, S. M., & Prieto, M. A. 1992, MNRAS, 258, 483
Whittet, D. C. B. 1992, Dust in the Galactic Environment (Bristol: IOP)